Available online at www.sciencedirect.com
ScienceDirect
Earth and Planetary Science Letters 249 (2006) 148 – 161
EPSL
www.elsevier.com/locate/epsl

The influence of natural radiation damage on helium diffusion kinetics in apatite

David L. Shuster *, Rebecca M. Flowers, Kenneth A. Farley

Division of Geological and Planetary Science, MC 100–25, California Institute of Technology, Pasadena, CA 91125, USA

Received 4 May 2006; received in revised form 11 July 2006; accepted 12 July 2006
Available online 21 August 2006
Editor: R.W. Carlson

Abstract

Stepwise degassing diffusion experiments on 39 different apatite samples using radiogenic ^{4}He and proton-induced ^{3}He reveal a range in closure temperature (T_c) from ~ 50 to 115 °C, for a cooling rate of 10 °C/Myr. There is no correlation between helium diffusion and apatite chemistry including F/Cl ratio, but the closure temperature is positively correlated with the radiogenic ^{4}He concentration ([^{4}He]) in each sample. We argue that [^{4}He] is a proxy for a sample's natural exposure to actinide radioactivity below the closure temperature, and that helium diffusion in apatite is impeded by radiation-induced damage to the apatite structure. The kinetics must therefore be an evolving function of time; measured diffusivities thus reflect a snapshot in time and cannot alone be applied to the thermochronometric interpretation of a given sample. The effect of radiation damage on helium diffusion appears to far exceed other known controls on helium diffusivity, including grain size.

Our diffusion data are well described by a previously proposed, quantitative model that consists of two Arrhenius relations, one for volume diffusion through undamaged mineral structure and one for release of helium from radiation damage "traps." The unknown parameters in this "trapping model" were determined from the diffusion experiments, and allow us to develop a tentative mathematical function that relates diffusivity to temperature and [^{4}He]. By inserting this function into a ^{4}He production-diffusion model we have explored how these results affect the interpretation of apatite (U–Th)/He thermochronometry. The model predicts that the effective ^{4}He closure temperature of apatite will vary with cooling rate and effective U concentration (eU) and may differ from the commonly assumed T_c of 70 °C by up to ±15 °C. The ^{4}He partial retention zone will look similar to previous expectations, but its depth will depend on accumulation time and on eU. Most notably, samples subjected to reheating after accumulation of substantial radiation damage will be more retentive than previously expected. These predictions are consistent with recent observations of unexpected apatite (U–Th)/He ages in some settings.

Keywords: Diffusion kinetics; (U–Th)/He; Thermochronometry; Radiation damage; Apatite; Helium

1. Introduction

One of the fundamental assumptions of noble gas thermochronometry is that diffusion kinetics of the radiogenic daughter measured in the laboratory can be

---

* Corresponding author. Now at: Berkeley Geochronology Center, 2455 Ridge Road, Berkeley, CA 94709, USA. Tel.: +1 510 644 9891; fax: +1 510 644 9201.

E-mail addresses: dshsuter@bgc.org (D.L. Shuster), rflowers@gps.caltech.edu (R.M. Flowers), farley@gps.caltech.edu (K.A. Farley).

0012-821X/$ - see front matter © 2006 Elsevier B.V. All rights reserved.
doi:10.1016/j.epsl.2006.07.028

extrapolated to the lower temperatures and longer timescales relevant in nature. This relies on the assertion that the physical mechanisms responsible for laboratory observations are *exactly* the same as those which occurred in nature throughout a sample's daughter accumulation history. Noble gas diffusivity is also commonly assumed to be solely a function of temperature. Due to the timescales of interest in geological problems, these are remarkably difficult assertions to evaluate. For instance, almost no geological context is known a priori with sufficient precision to rigorously validate the low-temperature extrapolations of laboratory-based diffusion kinetics. An alternative approach is to identify the chemical or physical variables which influence diffusion to ultimately develop a complete kinetic model of the diffusion process. Despite advances in quantifying diffusion kinetics with high precision, our physical understanding of noble gas diffusion remains relatively poor.

Over the last 10 yr, apatite (U–Th)/He chronometry has been increasingly applied for thermochronometry [1,2]. The abundance and spatial distribution of radiogenic ^{4}He within apatite is sensitive to cooling through temperatures found in the uppermost few kilometers of the Earth's crust. This makes the apatite (U–Th)/He chronometer useful for studying many problems in the Earth and planetary sciences, for instance involving tectonically driven crustal deformation and topographic evolution due to long-term erosion. With few exceptions, the diffusion kinetics of Durango apatite [3] has been used to interpret apatite (U–Th)/He ages: i.e., that the (U–Th)/He age represents time since the sample cooled through a closure temperature (T_c) of ~ 70 °C. This closure temperature was well constrained for Durango apatite and a few other samples in several early studies of helium diffusion [4–6].

Naturally occurring radioactivity can alter a mineral's structure by introducing isolated defects and vacancies [7,8]. The mechanism and rates at which radiation damage accumulates in crystals have been extensively studied in natural and ^{238}Pu-doped synthetic zircons and apatites to assess their potential as host phases for radioactive waste disposal [7,9–12]. In addition to ionizing elements through α- β- and γ-decays, actinide series decay also causes thousands of permanently displaced atoms primarily by direct impacts within cascades caused by heavy recoiled atoms during each alpha decay [10,13] and through atomic stopping of α particles and at a much lower frequency spontaneous U fission fragments (e.g., localized atomic displacements caused by ^{238}U fission in apatite create the measurable "fission tracks" commonly used for thermochronometry [14]). The rate at which α-decay induced damage accumulates in apatite and zircon is also a strong negative function of temperature; for apatite, damage accumulation rates are rapidly reduced at temperatures above 150 °C [12].

Previous work has recognized a role for radiation damage in controlling ^{4}He diffusion from minerals. For example, measured (U–Th)/He ages of very old zircon [15–17] and titanite crystals [15] indicate that ^{4}He loss is greatly accelerated at high degrees of radiation damage. Presumably the transformation of the crystalline matrix into an amorphous phase reduces impediments to helium mobility. In contrast, recent experiments demonstrate that synthetic radiation damage introduced by proton irradiation can impede helium diffusion in quartz [18]. Recent applications of percolation theory to study the radiation-induced transition of a crystal into an aperiodic state may provide insight to this apparent threshold behavior, where the overlapping of damaged regions occurs at the first percolation point [10,13]. However we are unaware of any systematic study of how helium diffusion kinetics responds to radiation damage, the goal of the present work.

Here, we present results that we hope will lead to a more complete physical model of helium diffusion in the mineral apatite ($Ca_5(PO_4)_3F$), and thus will aid in more accurate interpretation of (U–Th)/He thermochronometric data. Until the advent of ^{4}He/^{3}He thermochronometry [19], diffusion experiments relied on natural radiogenic ^{4}He in a sample. However this isotope will not generally have an initially uniform concentration distribution, an essential assumption for calculating diffusion coefficients [20]. In addition, many samples have insufficient ^{4}He to make accurate diffusion coefficients measurements, especially those with low degrees of integrated α-decay and hence radiation damage. By irradiating samples with high energy protons, it is possible to generate high concentrations of uniformly distributed ^{3}He for measuring diffusion coefficients with this isotope [21].

2. Methods

2.1. Samples

The samples investigated in this study come from many different localities and settings and were originally selected for ^{4}He/^{3}He thermochronometry rather than a systematic study of helium diffusion. Nevertheless, they span a wide range in cooling rate, (U–Th)/He age, lithology, and radioelement content. Specific sample designations and references are given in the caption to Table 1.

Table 1

Summary of helium diffusion kinetics in apatite

^{3}He	Sample	Locality	Reference	E_a (kJ/mol)	(+/−)	$\ln(D_o/a^2)$ ($\ln(s^{-1})$)	(+/−)	T_c (°C)	(+/−)	[^{4}He] (nmol/g)	He age (Ma)	[U] (ppm)	[Th] (ppm)	F/Cl (wt.%/wt.%)	(+/−)
	MC01-14	Tibet	[40]	119.5	2.0	10.2	0.5	46.8	8.6	1.1	7.5	28	32	514	108
	00MR-18	Southern Coast Mtns	UP	148.9	2.7	21.4	0.7	47.2	9.6	0.04	1.5	6	7	n.d.	n.d.
	CJ17	Cajon Pass, CA	[47]	122.3	2.9	11.1	0.6	47.9	11.5	0.2	6.0	6	9	69	5
	01MR59	Southern Coast Mtns	[23]	121.2	1.5	10.5	0.4	49.2	6.6	0.5	1.7	64	19	5	0.1
	CJ50	Cajon Pass, CA	[47]	120.5	0.9	10.2	0.2	49.4	3.7	0.0	0.0	33	38	108	6
	DYJS5	San Bernardino Mtns, CA	[46]	121.5	1.2	10.5	0.3	49.9	5.1	0.3	1.4	34	105	27	2.3
	03SS17	Sierra Nevada, CA	[41]	136.4	1.9	15.5	0.5	54.1	7.6	6.0	15.4	39	61	1043	385
	TEKI-38	Southern Coast Mtns	[23]	124.0	1.0	10.7	0.2	55.1	3.9	0.1	2.5	10	9	n.d.	n.d.
	TEKI-30	Southern Coast Mtns	[23]	123.2	1.0	10.2	0.3	56.5	4.7	0.4	4.7	18	16	n.d.	n.d.
	MC01-11	Tibet	[40]	125.4	1.6	10.9	0.4	57.3	6.9	1.1	8.2	28	15	711	91
	MC01-15	Tibet	[40]	127.7	1.6	11.4	0.6	59.7	8.3	2.7	6.2	70	33	35	10
	KC-1	Sierra Nevada, CA	[44][V]	129.5	3.8	12.0	0.9	60.2	15.8	5.8	31.0	47	32	n.d.	n.d.
	KC-9	Sierra Nevada	[44][V]	126.2	4.0	10.6	0.9	61.5	16.8	1.8	22.0	41	46	n.d.	n.d.
	0309GT	Sierra Nevada, CA	[41]	130.7	3.6	12.2	0.8	61.8	14.5	6.0	14.0	35	56	525	132
	L1	Bolivia	UP[III]	125.9	1.3	10.4	0.3	62.1	5.5	0.5	7.5	7	41	8	0.6
	TEKI-34	Southern Coast Mtns	[23]	130.9	3.0	12.1	0.7	63.0	12.4	0.2	3.7	15	6	n.d.	n.d.
	95MR17	Central Coast Mtns, Canada	[42]	129.4	1.8	11.4	0.4	64.1	7.4	1.4	9.5	26	19	18	1
	98MR-86	Central Coast Mtns, Canada	[42]	133.1	2.3	12.6	0.5	65.1	9.1	1.7	20.0	16	28	48	6
	SNLP	Sierra Nevada, CA	[41]	136.4	2.0	13.5	0.5	67.1	8.3	3.3	10.7	49	93	n.d.	n.d.
	MH96-14	Sierra Nevada, CA	[43]	133.3	1.3	12.2	0.3	68.3	5.3	10.8	56.6	34	22	129	22
	KC-10	Sierra Nevada, CA	[44][V]	134.0	3.4	12.1	0.8	70.8	14.2	5.7	23.0	36	41	n.d.	n.d.
	0316GT	Sierra Nevada, CA	[41]	129.6	2.1	10.4	0.5	71.7	9.1	8.2	22.0	60	53	59	8
	92TD118	Sierra Nevada, CA	UP[V]	134.1	1.1	12.0	0.3	71.8	4.9	3.2	n.d.	n.d.	n.d.	n.d.	n.d.
	92TD108	Sierra Nevada, CA	UP[V]	133.9	1.8	11.7	0.4	73.4	7.4	3.0	n.d.	n.d.	n.d.	n.d.	n.d.
	CJ12	Cajon Pass, CA	[47]	140.2	10.3	13.8	2.3	74.5	42.1	3.0	n.d.	n.d.	n.d.	n.d.	n.d.
	MH96-17	Sierra Nevada, CA	[43]	142.4	3.3	13.7	0.8	80.3	13.7	15.5	58.0	41	65	31	5

^{4}He	Sample	Locality	Reference	E_a	(+/−)	$\ln(D_o/a^2)$	(+/−)	T_c	(+/−)	[^{4}He]	He age	[U]	[Th]	F/Cl	(+/−)
	96MR56	Central Coast Mtns, Canada	[42]	109.2	0.8	6.6	0.2	44.1	3.7	0.4	5.6	17	1	n.d.	n.d.
	SG-7	San Gabriel Mtns, CA	[39]	132.4	0.8	12.3	0.2	65.4	3.7	1.3	7.6	27	65	n.d.	n.d.
	95MR17	Central Coast Mtns, Canada	[42]	125.4	2.1	9.5	0.5	67.3	9.2	1.4	9.5	26	19	n.d.	n.d.
	DYJS2	San Bernardino Mtns, CA	[46]	123.0	0.6	8.6	0.2	67.5	3.0	0.5	1.6	40	91	n.d.	n.d.
	96MR47	Central Coast Mtns, Canada	[42]	126.4	1.8	9.8	0.5	67.7	9.0	0.4	9.2	8	9	n.d.	n.d.
	TAM-1	Dry Valleys, Antarctica	UP	138.1	1.3	13.9	0.3	68.5	5.1	7.3	n.d.	n.d.	n.d.	n.d.	n.d.
	97MR48	Central Coast Mtns, Canada	[42]	129.3	0.7	10.5	0.2	70.2	3.5	0.7	9.5	14	9	n.d.	n.d.
	Durango	Mexico	[3]	139.7	0.5	14.0	0.1	71.7	1.9	8.2	31.0	8	180	13	0.8
	PRBH17	Big Horn Mtns, WY	[45]	125.1	3.8	8.0	0.9	77.8	17.5	26.2	107.0	24	137	n.d.	n.d.
	Tioga	Appalachians, PA	UP[II]	136.4	2.1	11.6	0.5	80.4	9.0	33.7	280.0	20	7	n.d.	n.d.
	WY1	Wind River Mtns, WY	UP[IV]	138.9	1.3	11.5	0.4	87.5	6.3	15.0	n.d.	n.d.	n.d.	n.d.	n.d.
	SZ00-196b	Snowbird, Canada	UP	139.7	1.3	9.3	0.3	106.8	5.9	30.0	850.0	10	5	n.d.	n.d.
	02-123a	Snowbird, Canada	UP	158.6	1.7	14.5	0.4	113.6	7.0	120.0	650.0	40	12	n.d.	n.d.
	Lake Mtn	Australia	UP[I]	140.6	3.8	8.5	0.9	116.0	18.1	236.0	329.0	146	3	n.d.	n.d.

Table references: [3,23,38–47].

All errors are reported as 1σ.

UP refers to a previously unpublished sample.

n.d. is not determined, nmol is 10^{-9} mol, wt.% is weight percent.

These designated samples were provided by: [I] Paul Green, [II] Ray Donelick, [III] Julie Libarkin, [IV] Pete Reiners, [V] Trevor Dumitru.

2.2. Experimental procedures

In this study, we conducted helium diffusion experiments following previously described procedures [5,21,22] using either proton-induced ^{3}He [21] or natural radiogenic ^{4}He as the diffusant. Artificial ^{3}He was created by irradiating samples with a 220 MeV proton beam generated by isochronous cyclotron acceleration and a fluence of 10^{15} protons/cm^2. Aliquots of single or multiple like-sized apatite crystals (average grain cross section was 120 μm) were held at a controlled temperature for a known time in a volume of ~ 300 cm^3 under static vacuum [22]. The thermally released helium was purified and cryogenically separated from other noble gases using activated charcoal held at 32 K and analyzed using either a sector-field mass spectrometer (^{3}He) or a quadrupole mass spectrometer (^{4}He). Using the fraction of ^{3}He or ^{4}He released and the duration of each step, we calculated the diffusion coefficient (D) normalized to the characteristic diffusive length scale a, (i.e., D/a^2) using published equations and the assumptions therein [20]. The estimated uncertainty on temperatures was better than ±2 °C and on diffusion coefficients better than ±0.2 natural log units ($\ln(\mathrm{s}^{-1})$).

We also determined major element chemistry for a subset of 14 samples using the Caltech JEOL 8200 electron microprobe (Supplementary table ST1). Apatites in polished grain mounts were analyzed using a 10 m spot size at 15 kV and 25 nA.

2.3. Arrhenius regression models

We quantified the temperature dependence of the diffusion coefficient from linear regression models of $\ln(D/a^2)$ against $1/T$ assuming the Arrhenius relationship $D(T)/a^2 = D_o/a^2 \exp(-E_a/RT)$, where E_a is the activation energy, and R is the gas constant. Our goal was to quantify the function $D(T)/a^2$ for each sample. For reasons discussed below, it was often not appropriate to use all experimental data for each linear regression. We therefore used data subsets to quantify diffusion kinetics.

2.3.1. Criteria for ^{3}He based experiments

We used the following criteria to establish data subsets for Arrhenius regression models for each ^{3}He based experiment: (i) we used the entire set of measured ^{3}He release fractions to calculate D/a^2 values; (ii) we excluded D/a^2 values from regression models for steps when $\Sigma F^3\mathrm{He} \leq 0.5\%$, and (iii) excluded values for temperatures ≥325 °C. Each experiment also yielded reproducible D/a^2 values at multiple, isothermal steps.

Diffusion coefficients calculated for the earliest steps in an experiment are sensitive to the influence of small fragments of apatite or other mineral dust adhered to the surface of an analyzed crystal. For instance, adhered material may have a very small diffusive length-scale, yet a proton-induced ^{3}He concentration equivalent to much larger grains. An adhered fragment would rapidly lose its gas at the beginning of an experiment and result in higher values of D/a^2 than appropriate for the analyzed crystal. Initially elevated values have previously been reported and typically represented less than 0.5% of the total ^{3}He abundances [18,21,23]. Fortunately, once the adhered fragments completely lose their gas, the calculated diffusivities rapidly converge upon appropriate values for a sample [21,24]. The previously observed ~ 0.5% threshold is consistent with the observations presented in this study. To avoid introducing bias towards higher diffusivity at low temperatures, we excluded these steps from each linear regression model.

In nearly every experiment, we observed an irreversible transition occurring ~ 325 °C towards shallower slopes on plots of $\ln(D/a^2)$ versus $1/T$. This transition has been well-documented in other apatites, and was interpreted as a change in diffusive mechanism beginning at ~ 325 °C [3]. We assumed that this behavior does not apply to lower temperatures, and excluded steps at temperatures ≥325 °C from each regression model. To minimize bias between samples, we used this threshold even if linearity persisted at temperatures above 325 °C.

Reproduced values of D/a^2 at a given temperature during sequential heating steps that (i) increased, (ii) decreased or (iii) remained constant in temperature verify that the assumed initial condition (i.e., a uniform spatial helium distribution within each crystal) was either accurate, or its inaccuracy had negligible influence on our results [3,21]. If calculated D/a^2 values accurately represent diffusion kinetics of a sample that is homogeneous with respect to D and a, they should be insensitive to a specific heating schedule. Due to differences in the expected spatial distributions of proton-induced ^{3}He and radiogenic ^{4}He, our specific criteria for selecting which steps we used in each linear regression model were somewhat different for each isotope. For instance, whereas we a priori expected the initial spatial distribution of proton-induced ^{3}He to be uniform, we could not reliably assume the same for natural ^{4}He since the spatial distributions of radiogenic ^{4}He were modified by direct α-particle emission and diffusion over geologic time [19].

2.3.2. Constraining diffusion kinetics from ^{4}He based experiments

Diffusion data using proton-induced ^{3}He were supplemented with ^{4}He diffusion data obtained on about a dozen additional samples. Here our approach to determining the diffusion parameters was more subjective than for ^{3}He because (i) the initial ^{4}He profile is unknown, so we can expect varying degrees of curvature in the early steps; and (ii) the experiments were performed over many years for different purposes and using varying heating schedules. As a consequence we were forced to choose a subset of the data from each experiment that maximized the number of steps included in the regression and gave the maximum linearity, again sensitive to the onset of curvature seen in the higher temperature steps. In some cases, particularly when helium retentivity was high, this required the use of steps above 325 °C. The results we obtained using ^{4}He are consistent with those obtained from ^{3}He (Fig. 1).

Previous results indicate that proton-induced ^{3}He and radiogenic ^{4}He yield nearly equivalent diffusion kinetics in Durango apatite despite the 25% fractional mass difference between these two isotopes [21]. If present in other samples, an isotopic difference in D of ~ 15% (i.e., predicted by the inverse root mass relationship) would superimpose a negligible bias to the result presented below. For instance a 15% difference in diffusivity would correspond to a difference in T_c of <1.5 °C (10 °C/Myr) in apatite.

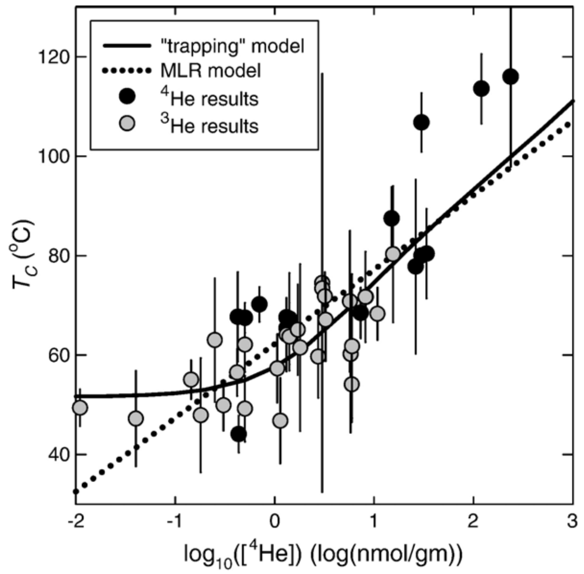

Fig. 1. Helium closure temperature (T_c) versus the log of the ^{4}He concentration (log$_{10}$([^{4}He]). Values of T_c were calculated for a cooling rate of 10 °C/Myr using the formulation of [25] for diffusion kinetics determined from stepwise release fractions of proton-induced ^{3}He (grey points) and natural radiogenic ^{4}He (black points). Complete datasets and the Arrhenius plots for each point are shown in the on-line Supplementary file. We estimated error bars on T_c (1σ; shown are vertical lines) solely from the linear regression statistics from the Arrhenius plots. The dotted line is the result of a multiple linear regression model of D/a^2 against both $1/T$ and log$_{10}$([^{4}He]) using the entire dataset (see Fig. 3). The solid curve is the calibrated "trapping" model discussed in Section 4.2.3 for best fit parameters: $E_a = 120$ kJ/mol, $E_t = 29$ kJ/mol, $D_o/a^2 = 1.58 \times 10^4$ s^{-1}, and $\psi = 1.26 \times 10^{-4}$ gm/nmol.

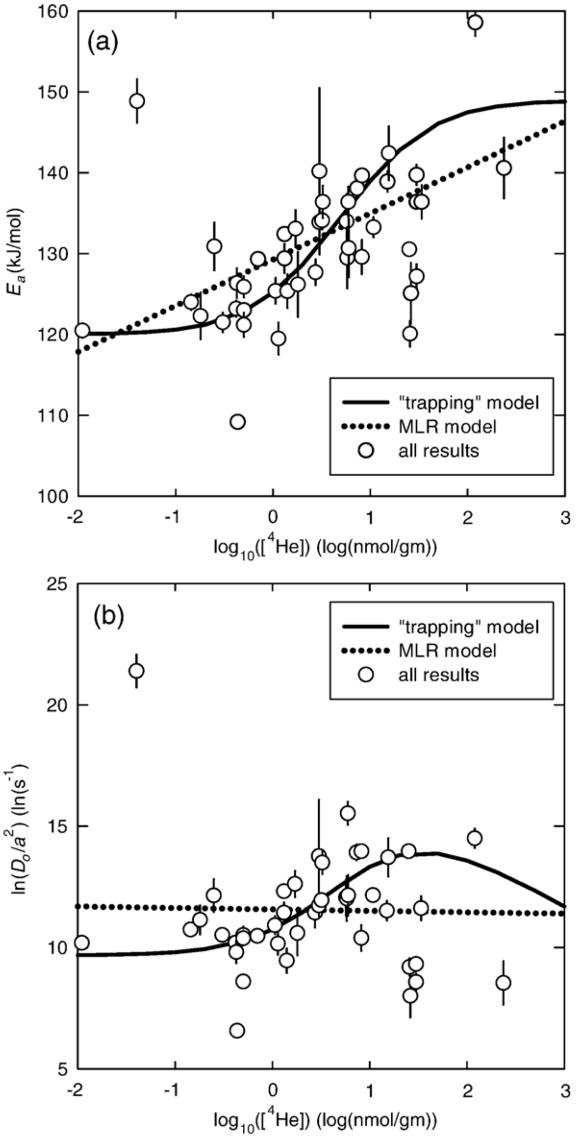

Fig. 2. Diffusion parameters. (a) The experimentally determined activation energy (E_a) and (b) the frequency factor (ln(D/a^2)) versus the log of the ^{4}He concentration (log$_{10}$([^{4}He]). We estimated error bars on each parameter (1σ; shown are vertical lines) solely from the linear regression statistics from the Arrhenius plots. The trapping model uses the best fit parameters listed in Fig. 1.

3. Results

3.1. Variance in the helium closure temperature T_c.

Table 1 summarizes the results of 40 helium diffusion experiments conducted on 39 different samples of apatite. Listed are the diffusion parameters D_o/a^2 and E_a with 95% confidence intervals estimated solely from regression statistics. Also reported is the closure temperature, T_c, calculated for a cooling rate of 10 °C/Myr [25], and the radiogenic ^{4}He concentration ([^{4}He]) naturally occurring in each sample. The complete sets of stepwise degassing data used to calculate the diffusion kinetics in Table 1 are presented as Arrhenius plots in supplementary Figs. S1 and S2. We found significantly larger variance in T_c (from 44 ± 4 °C to 116 ± 18 °C), than previously recognized for helium in apatite [3–6,26]. This variance in T_c is not a simple function of either E_a or D_o, but some combination (e.g., compare Figs. 1 and 2). For simplicity, the T_c is a single, relatively intuitive parameter which describes the diffusion kinetics and reveals differences relevant for thermochronometry.

3.2. Closure temperature versus F/Cl

Warnock et al. [4] suggested that F/Cl ratio might influence helium diffusivity from apatite, though the proposed differences were at the limit of their experimental precision. Our data seem to rule out this possibility. In the 16 samples for which we have chemical data (Table 1 and Supplementary table ST1), the R^2 correlation coefficient between F/Cl and T_c is statistically insignificant (0.08) even though the ratio spans a factor of more than 100 (from 5 ± 0.1 to 711 ± 91). Likewise, correlation between [F] and T_c is insignificant ($R^2 = 0.05$). Similarly, we observe no statistically significant correlations between T_c and other measured chemical parameters.

3.3. Closure temperature versus ^{4}He concentration

Fig. 1 shows a plot of T_c versus the radiogenic ^{4}He concentration, [^{4}He], of each sample. The ^{4}He concentrations vary over four orders of magnitude, reflecting differences in the uranium and thorium concentrations and the amount of time over which radiogenic ^{4}He accumulated in each sample. The significant correlation between T_c and the $\log_{10}$([^{4}He]) (correlation coefficient $R^2 = 0.64$) has not previously been documented.

4. Discussion

4.1. ^{4}He as a proxy for U and Th decay-induced damage

The central observation in our dataset is that helium closure temperature increases linearly with log([^{4}He]). This observation seems most logically attributed to the almost inescapable correlation between the ^{4}He concentration and U–Th decay-induced radiation damage to the apatite structure. A role for radiation damage in controlling helium diffusion from apatite was previously proposed to explain the apparent decrease in diffusivity at temperatures above ~ 265 °C observed in early experiments [3]. At secular equilibrium in both U and Th decay series, each alpha particle corresponds to a specific number of events causing damage, i.e., α- β- and γ- decays and spontaneous fission. In a system closed to ^{4}He loss and free of damage annealing, this demands correlation between the volume fraction of radiation damage in a crystal (v_{rd}) and the ^{4}He abundance: $v_{rd} \propto [^4\mathrm{He}]$. We expect the vast majority of crystal damage sites to be caused by α-decays, although each rare spontaneous fission events will cause a large number of atoms to be displaced. The parameter v_{rd} intrinsically weights these different processes accordingly.

However, since (i) ^{4}He can be lost by diffusion, (ii) the extent of cascade damage is sensitive to temperature, and (iii) structural damage can anneal, this relationship is an oversimplification. For instance, radiation damage can accumulate without retention of ^{4}He, i.e., at temperatures above T_c. Existing data suggest that the temperature threshold of radiation damage accumulation (T_{rda}) in apatite is greater than the helium T_c [12]. At temperatures above ~ 150 °C, the damage cascade in apatite is greatly diminished since the recovery rate of displaced atoms to their original sites is high. Therefore, samples which cooled more slowly from T_{rda} to T_c will have a higher ratio of $v_{rd}/[^4\mathrm{He}]$ than samples that more rapidly cooled through the same interval. Because annealing is also a strong function of temperature [27], there is a threshold above which all radiation damage will rapidly anneal. Perhaps not coincidentally, the threshold for preservation of fission induced damage in apatite (~ 110 ± 20 °C; [14]) is not much higher than the nominal helium T_c. The threshold for damage caused by α-decay should be comparable or lower. For this reason, we expect the influence of cooling rate on $v_{rd}/[^4\mathrm{He}]$ to be relatively minor in most cases, but it may contribute to the scatter observed in Fig. 1. Ultimately it might prove useful to directly measure structural damage using transmission electron microscopy rather than use ^{4}He as a proxy.

Previous experiments demonstrated that energetic proton irradiation had no measurable influence on the helium diffusion kinetics of several natural apatites containing radiogenic ^{4}He [21,26]. Therefore, in our analysis we have assumed that the proton irradiation induced a negligible amount of damage within all

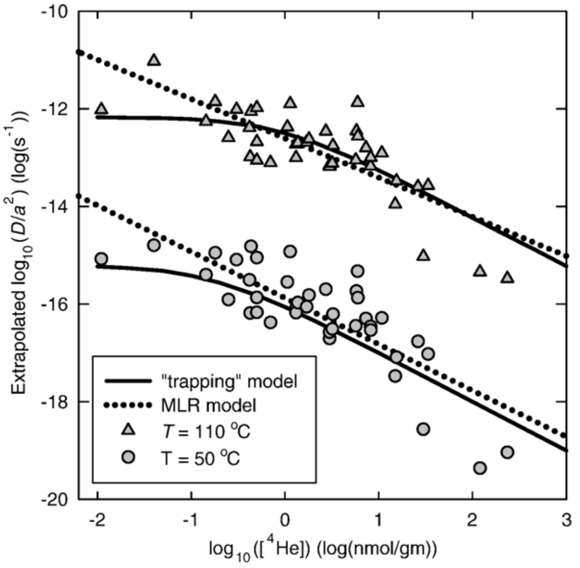

Fig. 3. Values of $\log_{10}(D/a^2)$ extrapolated to temperatures between 150 °C and 30 °C from the diffusion kinetics summarized in Table 1 plotted against the log of the ^{4}He concentration ($\log_{10}([^4\text{He}])$). Each point corresponds to the diffusion kinetics of a different sample extrapolated to 110 °C (triangles) and 50 °C (circles) as two examples. The dotted lines are the results of a multiple linear regression model of D/a^2 against both $1/T$ and $\log_{10}([^4\text{He}])$ using the entire dataset. The solid curves are the predictions of the quantitative "trapping model" (Eq. (3)) for the parameters used in Fig. 1.

samples. However, future experiments are required to fully evaluate this assumption, because the nuclear transmutations induced via energetic proton irradiation must cause additional damage to the crystal structure [28]. In samples with little or no natural radiation damage, the possibility remains that the energetic proton irradiation may have caused most or all of the radiation damage in the sample. This would cause the density of radiation damage to be higher than it would be if solely inferred from the measured radiogenic [^{4}He]. Indeed, we observe "elevated" T_c for the two samples with [^{4}He] <0.1 nmol/gm (Fig. 1). However, as we discuss below, the samples with "elevated" T_c at low [^{4}He] (i.e., an upper bound on the diffusion kinetics) are predicted by a simple mechanistic model.

4.2. Helium diffusion kinetics as an evolving function

The data shown in Fig. 1 imply that helium diffusion kinetics in apatite is an evolving property; the diffusion kinetics that we measure in the laboratory may not directly apply over all timescales. Thus, the helium diffusion kinetics quantified in an apatite today would *underestimate* its low-temperature diffusivity in the past. This means that at the time of interest (i.e., near the age of cooling), the effective ^{4}He closure temperature (T_{ec}) may in fact have been lower than what we observe today. If radiation-induced damage controls T_{ec}, then the accumulation of damage over time should cause diffusion kinetics to evolve at a predictable rate.

To explore how sensitive the apatite (U–Th)/He system is to this effect, we need a quantitative description of how the diffusion coefficient, D (i.e., rather than T_c), varies as a function of [^{4}He]. Fig. 2 shows how the Arrhenius diffusion parameters (E_a and D_o/a^2) each vary with $\log_{10}([^4\text{He}])$. Although correlation between E_a and [^{4}He] may be seen in some of the data (note center cluster of data in Fig. 2a), both E_a and D_o show significantly poorer correlation with $\log_{10}([^4\text{He}])$ (correlation coefficient $R^2=0.30$ and 0.0001, respectively) than with T_c. This may partly arise from the fact that we can better quantify diffusion coefficients and E_a at and closer to experimental temperatures than we can quantify D_o through extrapolation to infinite temperature. We first develop an empirical relationship between D and [^{4}He] using extrapolated values of D/a^2. We then adopt a mechanistic model, which we believe more accurately describes the physical phenomenon. We present each relationship below.

4.2.1. Multiple linear regression model

The temperature range most relevant for apatite (U–Th)/He thermochronometry is between 130 °C and Earth's surface temperatures. By extrapolating the Arrhenius relationships summarized in Table 1 (and shown in supplementary Figs. S1 and S2), we calculated values of D/a^2 for each sample between 150 °C and 30 °C at 20 °C intervals. Fig. 3 shows the extrapolated values at two of these temperatures plotted against the $\log_{10}([^4\text{He}])$ for all 39 samples, and clearly illustrates the covariance of D with both temperature and [^{4}He]: The diffusion coefficient is positively correlated with temperature and negatively correlated with [^{4}He]. At a given temperature, samples with higher [^{4}He] have lower diffusivity. To obtain an empirical description of this variability, we constructed a multiple linear regression model of $\log_{10}(D/a^2)$ against both $10^4/T$ and $\log_{10}([^4\text{He}])$. The results are plotted as dotted lines in Fig. 3 and given by the following relationship:

$$\log_{10}\left(\frac{D(T,[^4\text{He}])}{a^2}\right) = 5.025-0.026(\log_{10}([^4\text{He}]))-[0.675 + 0.030(\log_{10}([^4He]))]\cdot\left(\frac{10^4}{T}\right), \quad (1)$$

with T in units of Kelvin, [^{4}He] in nmol/gm, and $\log_{10}$ (D/a^2) is therefore in $\log_{10}(\mathrm{s}^{-1})$. Standard errors ($1\sigma$) on the four regression coefficients are (left to right) 0.33, 0.35, 0.01 and 0.01, respectively; the multiple R^2 value for this regression model is 0.94. Eq. (1) is valid between 150 °C and 30 °C and for $0.04 \geq [^4\mathrm{He}] \geq 240$ nmol/gm.

Fig. 1 and Fig. S3 illustrate how well this empirical model predicts the observed variations in diffusion kinetics. Using Eq. (1), we calculated T_c as a function of [^{4}He] for $\mathrm{d}T/\mathrm{d}t = 10$ °C/Myr (dotted line in Fig. 1). Fig. 1 and Fig. S3a show that although Eq. (1) generally describes the observed variance in T_c as a function of [^{4}He], in some cases the predicted closure temperature differs from the measured value by as much as 20 °C. Fig S3b shows that Eq. (1) typically predicts D/a^2 to within one order of magnitude of the observed values for all 39 samples between 150 °C and 30 °C.

Although Eq. (1) may adequately describe most of the observed variance in D, the linear regression model has two important limitations which restrict its applicability. The first is that the values of D/a^2 when extrapolated to low [^{4}He] appear unreasonably high for apatites with little or no radiation damage. For instance, the data in Fig. 1 show that apatite with lowest [^{4}He] (00MR-18) has significantly higher T_c than predicted by Eq. (1). The second limitation is that Eq. (1) provides no physical insight to the observed correlation, for instance why should the helium diffusion kinetics scale with the log of the [^{4}He]? Below, we expand upon a simple mechanistic model previously described by Farley [3] to explain the irreversible "rollover" in D/a^2 to lower values above ~ 265 °C in an Arrhenius plot, yet the model also predicts many of the observations presented in this study. This simple "trapping model" eliminates the two limitations above and predicts the observed log-linear relationship between T_c and [^{4}He].

4.2.2. Schematic trapping model

Several lines of evidence have been offered in support of the idea that radiation damage influences helium diffusion in minerals. For example, zircons which experienced exceptionally high α-particle fluences in nature ($>3\times10^{18}$ α/gm) had anomalously low (U–Th)/He ages [15–17]. Above this apparent dose threshold, metamicitzation is inferred to be so severe that ^{4}He retentivity *decreases* sharply due to "overlapping" of α-particle recoil damage zones [16,17]. If interconnected, a sufficiently high density of damage sites will create fast pathways for ^{4}He to reach the mineral surface and exit the system. However, the data shown in Fig. 1 suggest that higher exposures to natural radiation caused samples to become *more* retentive; self-irradiation appears to have caused helium retentivity to *increase*.

The possibility that radiation damage might impede diffusive loss from apatite was noted by Farley [3] as an explanation for the distinct curvature seen in ^{4}He diffusion Arrhenius plots. This model expands on that general idea. Fig. 4 illustrates a schematic "trapping model" of how isolated sites of radiation damage can decrease the net rate of helium mobility and therefore increase helium retentivity at a given temperature. Consider a ^{4}He atom that moves by diffusion a given distance within a crystal. In the absence of radiation-induced damage (Fig. 4a), the kinetics of this diffusion is solely a function of temperature. The rate that the free ^{4}He atom ($^4\mathrm{He}_f$) diffuses through the solid-state matrix will be controlled by the corresponding activation energy, E_a. This is the energy required of the ^{4}He atom to move from one interstitial site to another. Therefore, the net diffusion along the path shown in Fig. 4a will be described with a constant E_a.

Additional complexity will arise from the presence of a void space along the same path, for instance a site characterized by some number of displaced atoms within the crystalline matrix [29] (Fig. 4b). Since helium diffusion in apatite is nearly isotropic [3], isolated damage cascades may provide enough space between displaced atoms where ^{4}He atoms may accumulate at a lower energy state. If there is preferential partitioning into the damaged region, the ^{4}He atom will become locally "trapped" when it diffuses into the site. If the energy required for motion *within* the damaged site is lower than in the solid matrix, the behavior of the trapped atom ($^4\mathrm{He}_t$) will be more like a gas. This is analogous to a gas phase trapped inside a bubble within a solid, for instance a fluid inclusion. For the apatite (U–Th)/He system, we are ultimately interested in the net ^{4}He diffusion *out of* the mineral and the "effective" diffusivity which describes that entire process. Therefore, for the trapped ^{4}He atom to continue along the same path as in Fig. 4a and exit the mineral, it must overcome the energy barrier required to penetrate back into the crystalline matrix. This additional energy E_t is associated with partitioning of ^{4}He between the gas and solid phases. As discussed in [3,30], this partitioning will cause the effective diffusion coefficient for the material to decrease. The net effect of isolated void spaces is therefore to increase helium retentivity. As the volume density of radiation-induced damage increases over time, so also should the net helium retentivity increase (Fig. 4c). Only when the density of damage sites becomes sufficiently high that they form an interconnected network with each other

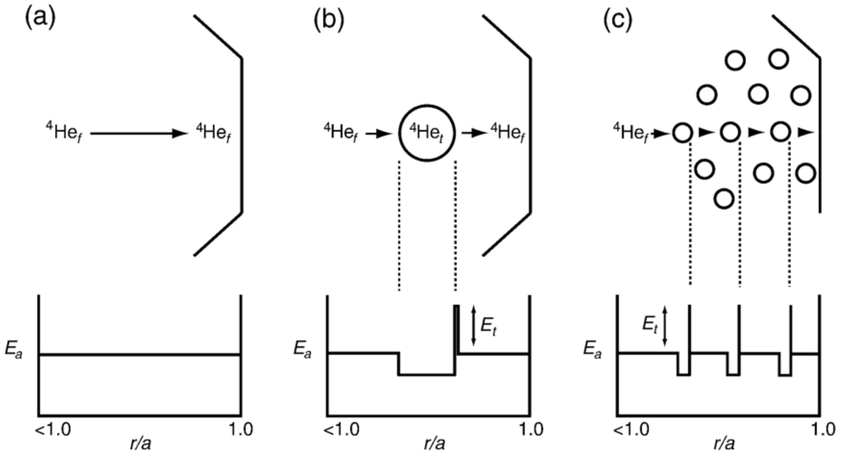

Fig. 4. A schematic model of the potential influence that isolated sites of radiation damage may have on helium diffusion kinetics. (a) Diffusion of a ^{4}He atom across a given distance in a mineral *without* radiation damage. (b) Diffusion of a ^{4}He atom across the same distance in a mineral *with* radiation damage; the circle represents a damage site. (c) The same as (b) after more sites of radiation damage accumulate. The upper panels are cartoons of the crystal with the ^{4}He atom motion due to diffusion indicated by the arrows in the vicinity of the crystal surface. Lower panels are plots of the effective activation energy for diffusion as a function of radial position, r, across a sphere of radius a; $r/a=1$ corresponds to the crystal surface. He_f is a “free” helium atom located within the undamaged crystal structure, He_t is a “trapped” atom located within a site of radiation damage. E_a is the activation energy for volume diffusion through regions of the crystal entirely free of radiation damage and E_t is the energy required of a helium atom to move out of a trap back into the undamaged crystal.

and the mineral’s surface (i.e., at the first percolation point when damage sites are no longer isolated [10,13]) will the net effect be to *decrease* retentivity.

4.2.3. Quantitative trapping model

Given that v_{rd} is the volume fraction of radiation damage sites in a crystal (in cm^3/cm^3; Fig. 4), then following Farley [3], $k_t{*}=k_t \cdot v_{rd}$, where k_t is defined as the partition ratio of helium “trapped” in sites of radiation damage to helium “free” to migrate through the matrix. Using these relationships, and following Crank [30], we find:

$$\frac{D(T,{}^4\mathrm{He})}{a^2}=\frac{\frac{D_o}{a^2}\cdot e^{\frac{-E_a}{RT}}}{k_t^{*}+1}=\frac{\frac{D_o}{a^2}\cdot e^{\frac{-E_a}{RT}}}{\left(k_o\cdot v_{rd}\cdot e^{\frac{E_t}{RT}}\right)+1}, \qquad (2)$$

where E_t is the energy barrier required of a helium atom to move out of a damage site back into an undamaged region and, D_o and E_a here describe helium diffusion through a crystalline matrix entirely free of radiation damage. If we then let η be a proportionality constant relating [^{4}He] to the volume fraction of damage sites (in dimensions gm/nmol) such that $v_{rd}=\eta\cdot[^4\mathrm{He}]$, Eq. (2) becomes:

$$\frac{D(T,{}^4\mathrm{He})}{a^2}=\frac{\frac{D_o}{a^2}\cdot e^{\frac{-E_a}{RT}}}{\left(k_o\cdot\eta\cdot[^4\mathrm{He}]\cdot e^{\frac{E_t}{RT}}\right)+1}, \qquad (3)$$

which relates D/a^2 to [^{4}He] at any point in time. By letting $\psi=k_o\cdot\eta$, the four free parameters for this expression are E_a, E_t, D_o, and ψ.

To determine the best-fit parameters to Eq. (3) we searched parameter space to minimize the misfit to observations. This was done as follows. First, a parameter set was selected, and for each sample with its associated [^{4}He] a plot of $\ln(D/a^2)$ versus $1/T$ was computed. When the effective activation energy is between E_a and E_a+E_t (e.g, for $0.1<[^4\mathrm{He}]<100$ nmol/gm; Fig. 2a) the trapping model yields a slightly curving array in this space, so we computed 10 values of $\ln(D/a^2)$ versus $1/T$ for T between 200 and 350 °C, i.e., the temperature range over which we actually measured helium diffusivity. These synthetic points were regressed, and the apparent values $\ln(D_o/a^2)$ and E_a were computed. These were then compared with observations on that sample, and the total error minimized weighting the two variables (E_a, D_o/a^2) for their variance. (Note that we excluded 5 samples which plot well away from the cluster of remaining samples). In addition, we required that the resulting range of $\ln(D_o/a^2)$ and E_a span the entire range observed in the dataset. A family of best-fit values were obtained, all of which yielded about the same degree of misfit and all of which yield essentially the same result upon forward modeling (see below).

4.3. Implications of the revised calibration for thermochronometry

If radiation damage impedes ^{4}He mobility, then the effective helium diffusion kinetics must change as an apatite evolves through time, and similarly must vary from apatite to apatite depending on the concentration of U and Th. As a result, neither the Dodson formulation for closure temperature [25] nor previous ^{4}He production-diffusion models which predict (U–Th)/He ages on arbitrary time-temperature paths [31] will yield accurate results. We can accommodate the radiation damage effect using a numerical model in which helium diffusivity obeys Eq. (3). Here we compare results of such a model with those obtained using the familiar Arrhenius diffusion parameters E_a and D_o when ignoring the radiation damage effect. The numerical model is based on one previously described [19,31].

In addition to Eq. (3), we must specify the grain size in the numerical model. This parameter is not explicit in Eq. (3) because all grains studied for diffusion were about the same size, roughly $a = 60$ μm. This is also the typical size of dated crystals. Thus grain size does not directly enter the diffusivity calculation, but it must be included to appropriately compute the effects of α-ejection-rounding on the ^{4}He concentration distribution [19,32]. We assumed $a = 60$ μm for this part of our modeling. For comparison, we also computed results using the standard Durango apatite kinetics [3], for the same grain size and including the effects of α ejection. As we show below, the effects of radiation damage on closure temperature far exceed the effects of grain size, at least for the range in grain size common to apatite.

To make the modeling quantitative we assumed six different effective uranium concentrations (eU = U + 0.235Th). Over the last several years we analyzed (U–Th)/He ages on ∼ 3500 apatites from many different rock types and localities, and these results guide our choice of eU values. In this population, the median eU is 28 ppm, and 95% of the apatites lie between 3.5 and 172 ppm. We therefore chose eU values of 4, 15, 28, 60, 100 and 150 ppm for illustration.

4.3.1. Monotonic cooling

The simplest time–temperature path to consider is monotonic cooling at a constant rate from an initial temperature well above that of ^{4}He retention. By comparing the modeled (U–Th)/He age with the temperature associated with that time in the past, it is possible to compute an "effective closure temperature", T_{ec}. In the case of a simple Arrhenius-type kinetics model, this procedure yields values identical to Dodson's equation [25]. We computed T_{ec} as a function of cooling rate and eU, as shown in Fig. 5. At rapid cooling rates the new model yields T_{ec} values lower than the Durango model. For example, at 10 °C/Myr the new model yields T_{ec} between 57 °C for the lowest eU apatite and 65 °C for the highest, compared with 72 °C for the Durango model. As cooling rate decreases, T_{ec} values for the different eU apatites become increasingly divergent, reflecting the greater time for radiation damage to build up and influence helium diffusion. For the same reason the T_{ec} values are less steeply sloped with cooling rate than the Durango model; as a result for all but the lowest eU apatite the T_{ec} values exceed those of the Durango model at a cooling rate of 0.1 °C/Myr.

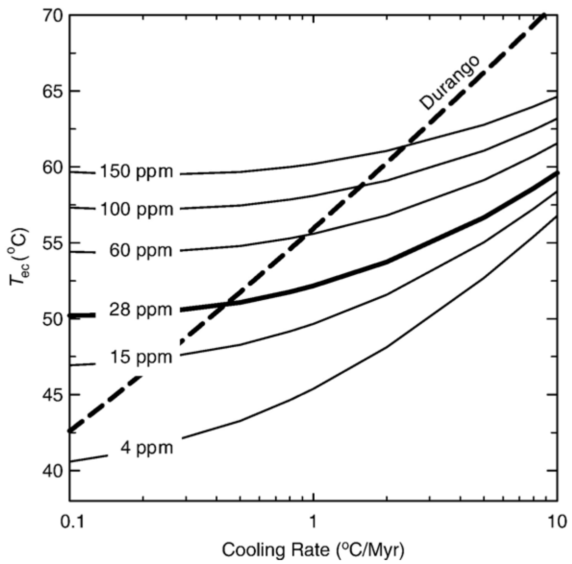

Fig. 5. Effective closure temperature as a function of cooling rate and eU (labeled in ppm) computed from the trapping diffusion model embedded in a ^{4}He production-diffusion model. Results for conventional Durango apatite kinetics are also shown. Simulated cooling paths began at 100 °C at various times selected to yield the reported cooling rates.

The major point of Fig. 5 is that apatite (U–Th)/He ages of monotonically cooled apatites are associated with effective closure temperatures that bracket the Durango model, but which may differ from that model by up to ∼ 15 degrees. Under fast cooling conditions, apatites transit the zone of partial ^{4}He retention fast enough that they acquire less radiation damage than occurs in the Durango sample, and hence their T_{ec} values are lower than for the standard Durango model. At lower cooling rates, as radiation damage accumulates and significantly retards diffusivity, the apatites yield higher T_{ec} values than the Durango model. The effect of radiation damage that we infer exceeds the only other known control on apatite helium diffusion: Grain size (i.e., a) influence on the quantity D_o/a^2 [3]. For example, at a cooling rate of 1 °C/Myr the modeled span of eU values is predicted to induce a total range in T_{ec} of about 17 °C; this is about twice as large as the T_{ec}

difference associated with a factor of two variation in grain size alone.

Many apatite (U–Th)/He datasets reveal linear age-elevation profiles. The slope of these arrays is commonly equated with exhumation rate, and this interpretation is unchanged by the proposed new diffusion model provided eU does not correlate with elevation. However variations in eU in the apatites comprising an age-elevation profile may cause scatter in the age-elevation relationships especially at low cooling rate, and this may provide a direct test of the new diffusion model. In addition, absolute amounts of exhumation are often estimated from the depth of the assumed closure isotherm. As shown in Fig. 5, that isotherm may be different than the ~ 70 °C usually assumed. The results also indicate that an evolving diffusion kinetics given by Eq. (3) will influence the sensitivity of ^{4}He/^{3}He thermochronometry, which we will explore in future studies.

4.3.2. The helium partial retention zone (HePRZ)

Fig. 6 illustrates a He partial retention zone (HePRZ [31]) calculated using Eq. (3). Results are shown for apatites held isothermally at a range of temperatures from 0 to 95 °C for 75 Myr. In general, the shape of the HePRZ is similar to and brackets that for the Durango model. At higher temperatures, ages tend to be lower than the Durango model, again reflecting the lower retentivity of less radiation-damaged apatite. Similarly, at lower temperatures the radiation damage builds up and hence the retentivity approaches and even exceeds that of Durango apatite, leading to an overall flattening of the HePRZ. For the median eU apatite, the HePRZ defined as the 10% and 90% points [31] ranges from 38 to 54 °C compared with 34 to 65 °C for Durango kinetics. The span in eU produces a spread of about 20 °C in the temperature at which He ages change most rapidly with temperature.

Fig. 6 thus predicts a HePRZ that looks similar to previous expectations and at a similar temperature range. The HePRZ model is most commonly invoked to explain a “break-in-slope” in an age elevation profile, commonly used to constrain the timing of a transition from slow to fast exhumation. This interpretation is unaffected by the new diffusion model. However the amount of exhumation, derived from the temperature for the lower temperature bound on the HePRZ and a presumed paleogeothermal gradient, will be lower with the radiation damage model than with the Durango model. For example, for a median eU apatite and a geothermal gradient of 20 °C/km, Fig. 6 implies about 500 m less exhumation to reveal the break in slope for the radiation model than for the Durango model. This effect is probably smaller than the errors associated with assuming a paleogeothermal gradient.

A borehole that has been isothermal (with no prior chance to accumulate radiation damage) and presently at known temperature could be used to test the radiation damage model, in particular to assess the slope of the age-depth trend (flatter in the radiation damage model) and the presence of eU correlated age variability. However, previous work on boreholes [4,33], or exhumed normal fault blocks that are thought to preserve a fossil HePRZ [34] lack sufficient sensitivity to apply such a test.

4.3.3. Reheating during burial

The previous two examples reveal that the radiation damage model yields ages that differ fairly modestly from those of the Durango model for isothermal and monotonically cooling conditions. However, the consequences of radiation-damage related changes in diffusivity can become extremely large for time–temperature paths that involve reheating, in which radiation damage first accumulates, and then ^{4}He is only partially lost. To illustrate this effect we considered an apatite that resides at 0 °C from 300 Myr to 200 Myr, during which radiation damage builds up, followed by heating to a maximum temperature (T_{pk}) between 0 and

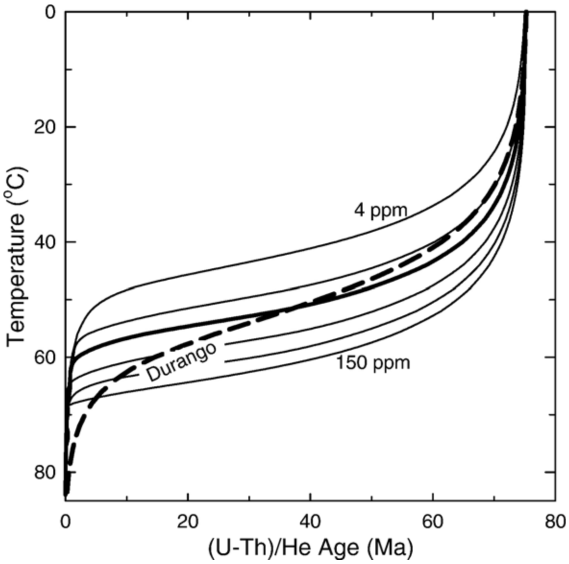

Fig. 6. The helium partial retention zone computed by assuming apatites of varying eU are held isothermally at the indicated temperatures for 75 Myr for the trapping diffusion model and conventional Durango apatite diffusion kinetics. Two curves are labeled with associated eU values (4, 150 ppm). Unlabelled curves are for 15, 28, 60, and 100 ppm eU from top to bottom.

100 °C at 100 Myr, followed by monotonic cooling to 0 °C at 0 Myr. This is a simplified example of what is expected to happen to detrital apatites subjected to burial heating.

As shown in Fig. 7, the consequences are profound and strongly correlated with eU. At low T_{pk}, all grains retain all of their helium, and hence all record an age of 300 Myr. Similarly, for T_{pk} values in excess of about 90 °C, all grains are "reset" and the difference in age simply reflects the difference in T_{ec} for the range of eU values at 1 °C/Myr, as shown in Fig. 5. However, at intermediate peak temperatures there is an enormous span in predicted (U–Th)/He age correlated with eU. At its most extreme at about 60 °C, the low eU grains are almost completely reset while the high eU grains are almost completely unaffected by diffusive loss. In this example, results of the Durango model plot through the middle of the swath, reflecting the fact that the model ^{4}He concentrations (and hence diffusivities) lie on either side of that measured on Durango apatite.

The key message of this figure is that burial reheating can be expected to yield extremely large degrees of age scatter, strongly correlated with eU. This is a very sensitive test of the role of radiation damage on helium diffusion and indeed the expected effect has been observed in several cases [35–38]. Importantly, this model predicts that apatite (U–Th)/He ages will not be significantly older than apatite fission track ages (Fig. 7) and thus does not offer an obvious explanation for cases in which "age reversal" is observed. However, results from this type of time–temperature path will be extremely sensitive to the kinetics of annealing of radiation damage and how ^{4}He mobility responds to annealing. Our model uses ^{4}He concentration as a proxy for damage, but clearly this is an oversimplification. Further study of annealing as it affects helium diffusion is required to accurately evaluate (U–Th)/He ages of apatites cooled on such paths.

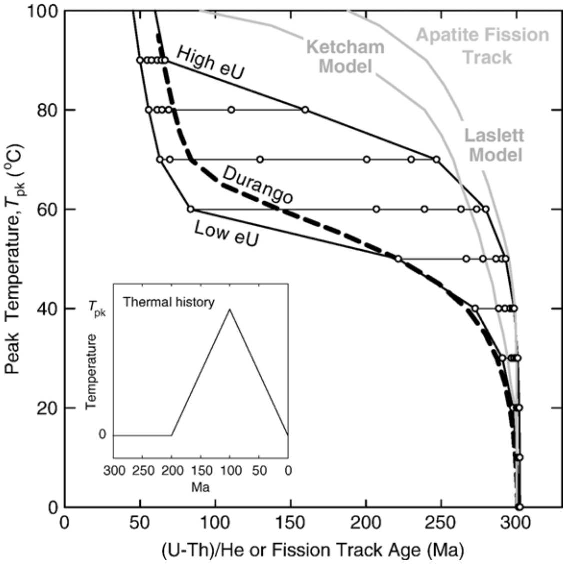

Fig. 7. The effects of reheating on (U–Th)/He ages using the trapping model as a function of eU and peak temperature achieved, compared with ages calculated assuming conventional Durango kinetics and apatite fission track ages computed from two annealing models in "HeFTy" program [48,49]. The model assumes samples are held at 0 °C from 300 to 200 Myr, followed by monotonic heating to peak temperature (T_{pk}) at 100 Myr, followed by monotonic cooling to 0 °C at 0 Myr (schematic cooling path shown in inset). Open symbols are computed points for various eU values (4, 15, 28, 60, 100, and 150 ppm from left to right on the figure).

5. Conclusions

Experimentally determined diffusion coefficients demonstrate that the closure temperature (T_c) for helium retention in apatite spans a wider range than previously recognized: From 44±4 °C to 116±18 °C and correlates with the radiogenic ^{4}He abundance in a given sample. We argue that the radiogenic ^{4}He concentration ([^{4}He]) is a measurable proxy for the U- and Th-decay series radiation damage that accumulated within each crystal over geologic time. As the volume density of structural damage increases, apatite becomes more helium retentive. This implies that helium retentivity, and hence the effective helium diffusion kinetics, is an evolving function of time. Calibrated with diffusion kinetics of 39 different apatite samples, we present a simple, quantitative "trapping model" which relates diffusivity to both temperature *and* [^{4}He]. Here [^{4}He] is an indirect but only approximate indicator of the volume fraction of radiation damage. The simple model predicts the observed log-linear correlation between T_c and [^{4}He]. By inserting this function into a ^{4}He production-diffusion calculation, the "trapping model" for diffusion kinetics predicts: (i) that the effective ^{4}He closure temperature of apatite will vary with cooling rate *and* effective U concentration (eU) and may differ from 70 °C by up to ±15 °C, (ii) the depth of the ^{4}He partial retention zone will depend on accumulation time and on eU, and (iii) samples subjected to reheating after accumulation of substantial radiation damage will be more retentive than previously expected.

Acknowledgement

We thank the many people who (inadvertently) provided samples for this study and those who participated in the field work to collect them. We thank Anne Blythe, Marin Clark, Todd Ehlers, Martha

House, Margi Rusmore, Jim Spotila, Rich Wolf and in particular Ray Donelick, Trevor Dumitru, Paul Green, Julie Libarkin and Pete Reiners who provided samples where the (U–Th)/He results have not been published elsewhere. We also thank Lindsey Hedges for the help with sample preparation. We appreciate two very helpful reviews by an anonymous referee and Peter Zeitler. This work was supported by NSF grant 0408526 to KAF.

Appendix A. Supplementary data

Supplementary data associated with this article can be found, in the online version, at doi:10.1016/j.epsl.2006.07.028.

References

[1] K.A. Farley, (U–Th)/He dating: techniques, calibrations, and applications, Noble Gases in Geochemistry and Cosmochemistry, 2002, pp. 819–844.

[2] P.W. Reiners, T.A. Ehlers, P.K. Zeitler, Past, present, and future of thermochronology, Low-Temperature Thermochronology: Techniques, Interpretations, and Applications, 2005, pp. 1–18.

[3] K.A. Farley, Helium diffusion from apatite: general behavior as illustrated by Durango fluorapatite, J. Geophys. Res. 105 (2000) 2903–2914.

[4] A.C. Warnock, et al., An evaluation of low-temperature apatite U–Th/He thermochronometry, Geochim. Cosmochim. Acta 61 (24) (1997) 5371–5377.

[5] R.A. Wolf, K.A. Farley, L.T. Silver, Helium diffusion and low-temperature thermochronometry of apatite, Geochim. Cosmochim. Acta 60 (21) (1996) 4231–4240.

[6] P.K. Zeitler, et al., U–Th-He dating of apatite: a potential thermochronometer, Geochim. Cosmochim. Acta 51 (1987) 2865–2868.

[7] R.C. Ewing, W.J. Weber, J.F.W. Clinard, Radiation effects in nuclear waste forms for high-level radioactive waste, Prog. Nucl. Energy 29 (2) (1995) 63–127.

[8] W.J. Weber, et al., Radiation effects in crystalline ceramics for the immobilization of high-level nuclear waste and plutonium, J. Mater. Res. 13 (6) (1998) 1434–1484.

[9] W.J. Weber, R.C. Ewing, L.M. Wang, The radiation-induced crystalline-to-amorphous transition in zircon, J. Mater. Res. 9 (3) (1994) 688–698.

[10] S. Rios, et al., Amorphization in zircon: evidence for direct impact damage, J. Phys., Condens. Matter 12 (11) (2000) 2401–2412.

[11] R.C. Ewing, et al., Radiation effects in zircon, Zircon, 2003, pp. 387–425.

[12] W.J. Weber, R.C. Ewing, A. Meldrum, The kinetics of alpha-decay-induced amorphization in zircon and apatite containing weapons-grade plutonium or other actinides, J. Nucl. Mater. 250 (2–3) (1997) 147–155.

[13] K. Trachenko, M.T. Dove, E.K.H. Salje, Structural changes in zircon under alpha-decay irradiation, Phys. Rev., B 65 (18) (2002).

[14] R.A. Donelick, P.B. O'Sullivan, R.A. Ketcham, Apatite fission-track analysis, Low-Temperature Thermochronology: Techniques, Interpretations, and Applications, 2005, pp. 49–94.

[15] Hurley, P.M., The helium age method and the distribution and migration of helium in rocks, i.F. Hurley PM (1954) The helium age method and the distribution and migration of helium in rocks, H., ed., Nuclear Geology: New York, John Wiley and Sons, p. 301–329., Editor. 1954.

[16] L. Nasdala, et al., Incomplete retention of radiation damage in zircon from Sri Lanka, Am. Mineral. 89 (1) (2004) 219–231.

[17] P.W. Reiners, et al., (U–Th)/(He–Pb) double dating of detrital zircons, Am. J. Sci. 305 (4) (2005) 259–311.

[18] D.L. Shuster, K.A. Farley, Diffusion kinetics of proton-induced ^{21}Ne, ^{3}He, and ^{4}He in quartz, Geochim. Cosmochim. Acta 69 (9) (2005) 2349–2359.

[19] D.L. Shuster, K.A. Farley, ^{4}He/^{3}He thermochronometry, Earth Planet. Sci. Lett. 217 (1–2) (2004) 1–17.

[20] H. Fechtig, S. Kalbitzer, The diffusion of argon in potassium bearing solids, in: O.A. Schaeffer, J. Zahringer (Eds.), Potassium–Argon Dating, Heidelberg, Springer, 1966, pp. 68–106.

[21] D.L. Shuster, et al., Quantifying the diffusion kinetics and spatial distributions of radiogenic ^{4}He in minerals containing proton-induced ^{3}He, Earth Planet. Sci. Lett. 217 (1–2) (2004) 19–32.

[22] K. Farley, P. Reiners, V. Nenow, An apparatus for high-precision helium diffusion measurements from minerals, Anal. Chem. 71 (1999) 2059–2061.

[23] D.L. Shuster, T.A. Ehlers, M.E. Rusmore, K.A. Farley, Rapid glacial erosion at 1.8 Ma revealed by ^{4}He/^{3}He thermochronometry, Science 310 (5754) (2005) 1668–1670.

[24] P.W. Reiners, K.A. Farley, Helium diffusion and (U–Th)/He thermochronometry of titanite, Geochim. Cosmochim. Acta 63 (1999) 3845–3859.

[25] M.H. Dodson, Closure temperatures in cooling geological and petrological systems, Contrib. Mineral. Petrol. 40 (1973) 259–274.

[26] D.L. Shuster, K.A. Farley, ^{4}He/^{3}He Thermochronometry: theory, practice and potential complications, in: P.W. Reiners, T.A. Ehlers (Eds.), Low-temperature thermochronology: techniques, interpretations, and applications, Mineralogical Society of America, Washington, D.C., 2005, pp. 181–202.

[27] P. Green, et al., Thermal annealing of fission tracks in apatite: 1. A qualitative description, Chem. Geol. 59 (1986) 237–253.

[28] B.X. Gu, et al., The effect of H+ irradiation on the Cs-ion exchange capacity of zeolite–NaY, J. Mater. Chem. 10 (11) (2000) 2610–2616.

[29] A. Meldrum, L.M. Wang, R.C. Ewing, Electron-irradiation-induced phase segregation in crystalline and amorphous apatite: a TEM study, Am. Mineral. 82 (9–10) (1997) 858–869.

[30] J. Crank, The Mathematics of Diffusion, 2nd ed. Oxford University Press, New York, 1975 414.

[31] R.A. Wolf, K.A. Farley, D.M. Kass, Modeling of the temperature sensitivity of the apatite (U–Th)/He thermochronometer, Chem. Geol. 148 (1998) 105–114.

[32] K.A. Farley, R.A. Wolf, L.T. Silver, The effects of long alpha-stopping distances on (U–Th)/He ages, Geochim. Cosmochim. Acta 60 (1996) 4223–4229.

[33] M.A. House, et al., Evaluating thermal history models for the Otway Basin, southeastern Australia, using (U–Th)/He and fission-track data from borehole apatites, Tectonophysics 349 (1–4) (2002) 277–295.

[34] D.F. Stockli, K.A. Farley, T.A. Dumitru, Calibration of the apatite (U–Th)/He thermochronometer on an exhumed fault block, White Mountains, California, Geology 28 (11) (2000) 983–986.

[35] P.D. Crowley, et al., Laramide exhumation of the Bighorn Mountains, Wyoming: an apatite (U–Th)/He thermochronology study, Geology 30 (1) (2002) 27–30.

[36] R.M. Flowers, et al., Radiation damage control on apatite (U–Th)/He dates from the Grand Canyon region, Colorado Plateau. Geology, 2006. In Review.

[37] P.F. Green, I.R. Duddy, Interpretation of apatite (U-Th)/He ages and fission track ages from cratons, Earth Planet. Sci. Lett. 244 (2006) 541–547.

[38] J.A. Spotila, et al., Origin of the Blue Ridge escarpment along the passive margin of Eastern North America, Basin Res. 16 (1) (2004) 41–63.

[39] A.E. Blythe, et al., Structural and topographic evolution of the central Transverse Ranges, California, from apatite fission-track, (U–Th)/He and digital elevation model analyses, Basin Res. 12 (2) (2000) 97–114.

[40] M.K. Clark, et al., Late Cenozoic uplift of southeastern Tibet, Geology 33 (6) (2005) 525–528.

[41] M.K. Clark, et al., The non-equilibrium landscape of the southern Sierra Nevada, California, GSA Today 15 (9) (2005) 4–10.

[42] K.A. Farley, M.E. Rusmore, S.W. Bogue, Post-10 Ma uplift and exhumation of the northern coast mountains, British Columbia, Geology 29 (2) (2001) 99–102.

[43] M.A. House, B.P. Wernicke, K.A. Farley, Paleo-geomorphology of the Sierra Nevada, California, from (U–Th)/He ages in apatite, Am. J. Sci. 301 (2) (2001) 77–102.

[44] M.A. House, et al., Cenozoic thermal evolution of the central Sierra Nevada from (U–Th)/He thermochronometry, Earth Planet. Sci. Lett. 151 (1997) 167–179.

[45] P.W. Reiners, K.A. Farley, Influence of crystal size on apatite (U–Th)/He thermochronology: an example from the Bighorn mountains, Wyoming, Earth Planet. Sci. Lett. 188 (2001) 413–420.

[46] J.A. Spotila, et al., Near-field transpressive deformation along the San Andreas fault zone in southern California, based on exhumation constrained by (U–Th)/He dating, J. Geophys. Res., [Solid Earth] 106 (B12) (2001) 30909–30922.

[47] R.A. Wolf, Development of the (U–Th)/He thermochronometer, Division of Geological and Planetary Sciences, California Institute of Technology, Pasadena, CA, 1996, p. 212.

[48] T.A. Ehlers, et al., Computational tools for low-temperature thermochronometer interpretation, Low-Temperature Thermochronology: Techniques, Interpretations, and Applications, 2005, pp. 589–622.

[49] R.A Ketcham, Forward and inverse modeling of low-temperature thermochronometry data, Low-Temperature Thermochronology: Techniques, Interpretations, and Applications, 2005, pp. 275–314.

Supplementary file for:

“The influence of natural radiation damage on helium diffusion kinetics in apatite.”

by

David L. Shuster[1,2,]*, Rebecca M. Flowers[1], Kenneth A. Farley[1]

[1]*Division of Geological and Planetary Science, MC 100-25, California Institute of Technology, Pasadena, CA 91125, USA*

[2]Now at: *Berkeley Geochronology Center, 2455 Ridge Road, Berkeley, CA 94709, USA*

*Corresponding author. Tel.: +1-510-644-9891; Fax: +1-510-644-9201

E-mail addresses:
dshsuter@bgc.org (D.L. Shuster),
rflowers@gps.caltech.edu (R.M. Flowers),
farley@gps.caltech.edu (K.A. Farley)

This 44 page file contains the following:

Supplementary Figure Captions

Fig. S1 Arrhenius plots for the 26 experiments using proton-induced ^{3}He as the diffusant. Open circles are the diffusion coefficients, D, normalized to the diffusive length scale, a, calculated [1] from release fractions of proton-induced ^{3}He [2]. Solid black line is the inferred helium diffusion kinetics determined by linear regression to a subset array (indicated as black circles) selected using the criteria discussed in the main text.

Fig. S2 Arrhenius plots for 13 experiments using radiogenic ^{4}He as the diffusant. Open circles are the diffusion coefficients, D, normalized to the diffusive length scale, a, calculated [1] from release fractions of ^{4}He. Solid black line is the inferred helium diffusion kinetics determined by linear regression to a subset array (indicated as black circles) selected using the criteria discussed in the main text.

Fig. S3 A comparison of the experimentally determined values for each sample with the predicted values calculated from the multiple linear regression model shown in Eq. 1 (i.e., $D/a^2 = \mathrm{f}(T, [^4\mathrm{He}])$). **(a)** The closure temperature (T_c). **(b)** Values of $\log_{10}(D/a^2)$ extrapolated to and calculated for temperatures between 150 ^{o}C and 30 ^{o}C at 20 ^{o}C intervals. Lines are slope 1.

Fig. S4 A comparison of the experimentally determined values for each sample with the predicted values calculated from the quantitative “trapping model” shown in Eq. 3 for best fit parameters: E_a = 120 kJ/mol, E_t = 29 kJ/mol, $D_o = 1.58\times10^4$ s^{-1}, and $\psi = 1.26\times10^{-4}$ gm/nmol.. **(a)** The closure temperature (T_c). **(b)** Values of $\log_{10}(D/a^2)$ extrapolated to and calculated for temperatures between 150 ^{o}C and 30 ^{o}C at 20 ^{o}C intervals. Lines are slope 1.

References:

1. Fechtig, H. and S. Kalbitzer, *The diffusion of argon in potassium bearing solids*, in *Potassium-Argon Dating*, O.A. Schaeffer and J. Zahringer, Editors. 1966, Springer: Heidelberg. p. 68-106.
2. Shuster, D.L., et al., *Quantifying the diffusion kinetics and spatial distributions of radiogenic ^{4}He in minerals containing proton-induced ^{3}He.* Earth and Planetary Science Letters, 2004. 217(1-2): p. 19-32.

Table ST1: Electron probe data.

Sample	CaO	(+/-)	P_2O_5	(+/-)	FeO	(+/-)	MnO	(+/-)	F	(+/-)	Cl	(+/-)	T_c (^{o}C)	(+/-)
01MR-59	53.92	0.05	40.53	0.10	0.09	0.00	0.07	0.00	4.17	0.05	0.77	0.01	49.2	6.6
L1	53.68	0.12	40.34	0.19	0.10	0.01	0.12	0.00	4.35	0.27	0.52	0.01	62.1	5.5
Durango	53.34	0.11	40.10	0.16	0.03	0.01	0.00	0.00	5.51	0.36	0.43	0.00	71.7	1.9
95MR-17	54.54	0.14	40.85	0.14	0.02	0.00	0.06	0.02	4.09	0.20	0.23	0.01	67.3	9.2
DYJS-5	54.33	0.08	41.01	0.11	0.02	0.01	0.06	0.00	5.03	0.27	0.19	0.01	49.9	5.1
MH96-17	54.37	0.27	40.79	0.54	0.14	0.12	0.08	0.01	4.54	0.05	0.15	0.02	80.3	13.7
MC01-15	54.54	0.08	40.58	0.18	0.02	0.00	0.06	0.02	4.70	0.15	0.13	0.04	59.7	8.3
98mr-86	54.15	0.19	40.32	0.09	0.03	0.01	0.07	0.01	4.59	0.10	0.10	0.01	65.1	9.1
0316GT	54.23	0.12	40.55	0.15	0.04	0.01	0.09	0.01	4.62	0.16	0.08	0.01	71.7	9.1
cj17	54.47	0.14	40.72	0.22	0.05	0.02	0.06	0.01	4.96	0.26	0.07	0.00	47.9	11.5
cj50	54.46	0.09	40.72	0.05	0.02	0.02	0.05	0.00	5.22	0.28	0.05	0.00	49.4	3.7
MH96-14	54.49	0.02	41.01	0.05	0.01	0.00	0.09	0.02	5.26	0.14	0.04	0.01	68.3	5.3
MC01-14	54.83	0.15	41.13	0.15	0.02	0.01	0.07	0.01	5.33	0.03	0.01	0.00	46.8	8.6
0309GT	54.42	0.02	40.73	0.04	0.01	0.01	0.09	0.01	5.52	0.36	0.01	0.00	61.8	14.5
MC01-11	54.50	0.13	41.30	0.11	0.01	0.01	0.10	0.03	5.61	0.23	0.01	0.00	57.3	6.9
03SS17	54.41	0.08	40.77	0.16	0.03	0.00	0.07	0.01	5.42	0.16	0.01	0.00	54.1	7.6

All chemical data is reported as weight percent with 1σ analytical uncertainties.

Supplementary figures for "The influence of natural radiation damage on helium diffusion kinetics in apatite"

Figure S1-
1 of 26

Helium-3 experiment

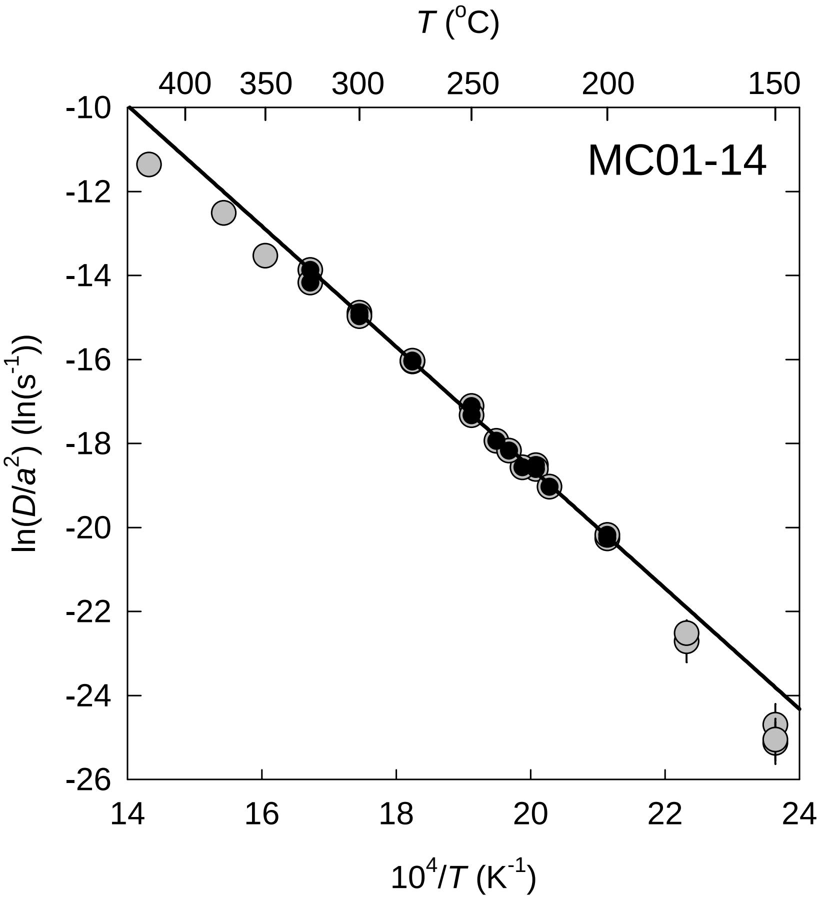

Figure S1-
2 of 26

Helium-3 experiment

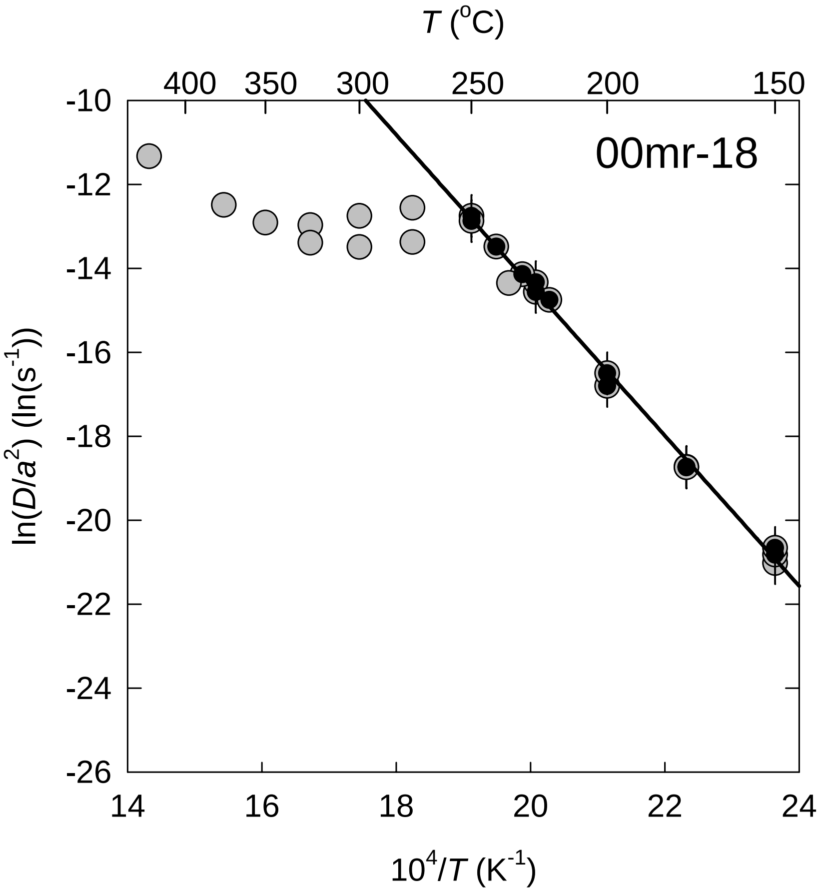

Supplementary figures for "The influence of natural radiation damage on helium diffusion kinetics in apatite"

Figure S1-
3 of 26

Helium-3 experiment

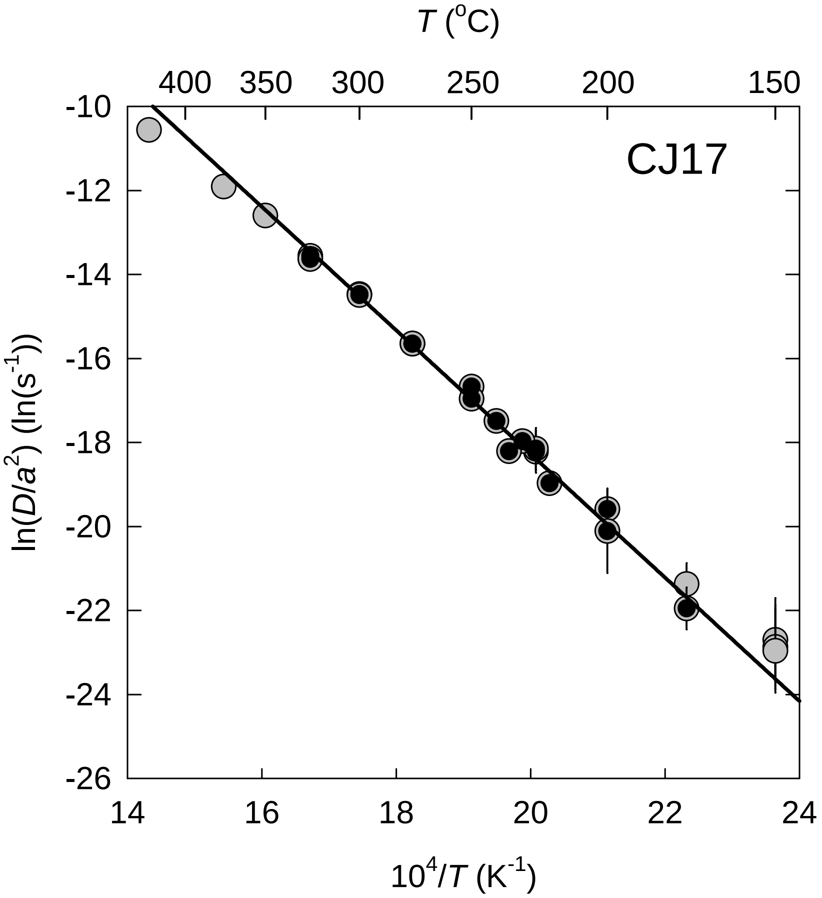

Supplementary figures for "The influence of natural radiation damage on helium diffusion kinetics in apatite"

Figure S1-
4 of 26

Helium-3 experiment

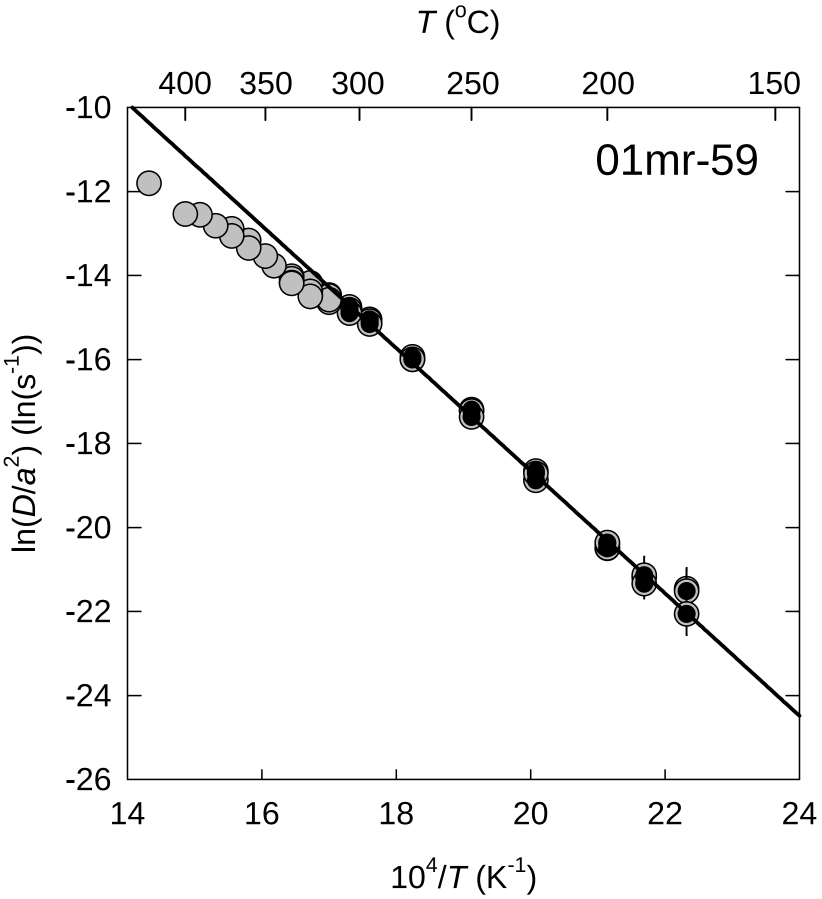

Figure S1-
5 of 26

Helium-3 experiment

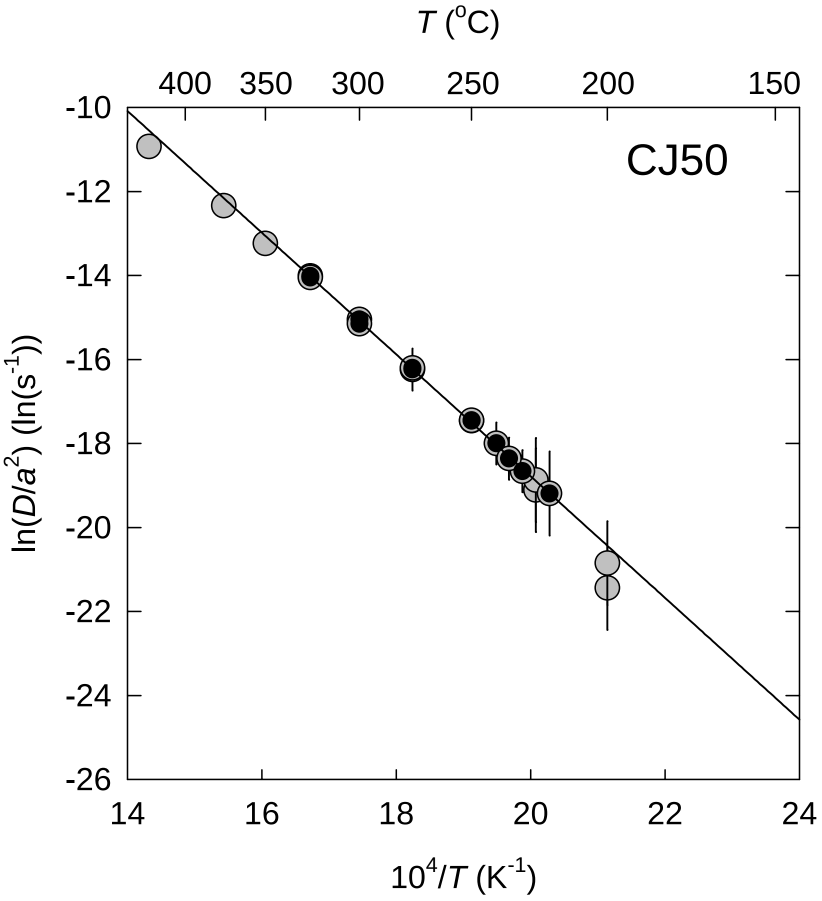

Figure S1-
6 of 26

Helium-3 experiment

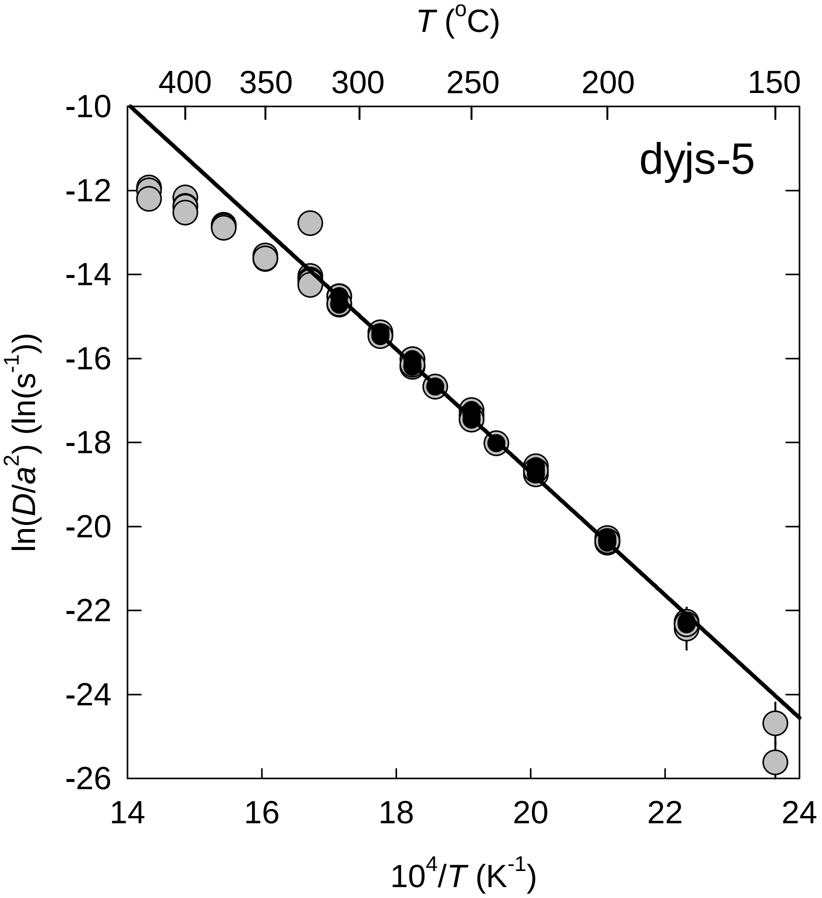

Figure S1-
7 of 26

Helium-3 experiment

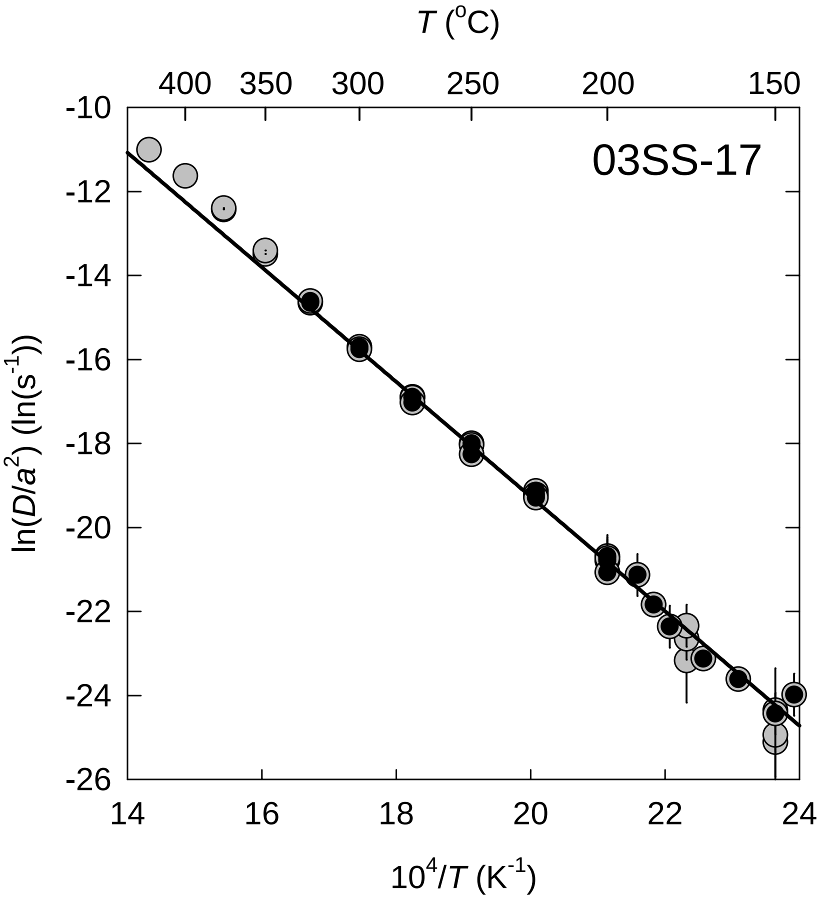

Supplementary figures for "The influence of natural radiation damage on helium diffusion kinetics in apatite"

Figure S1-
8 of 26

Helium-3 experiment

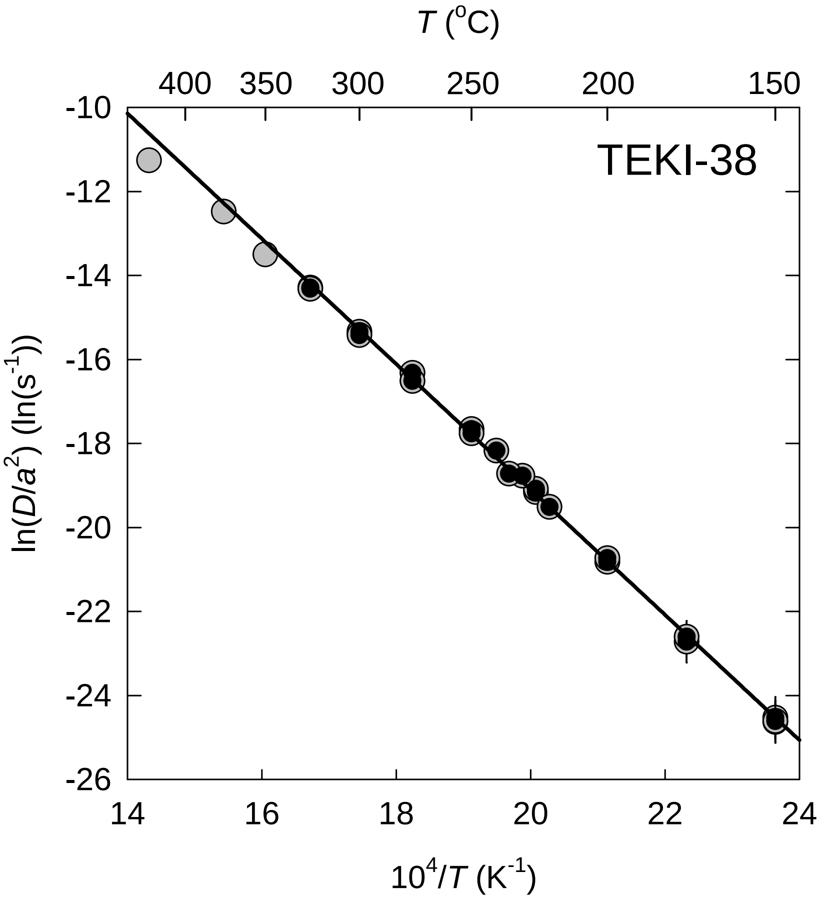

Supplementary figures for "The influence of natural radiation damage on helium diffusion kinetics in apatite"

Figure S1-
9 of 26

Helium-3 experiment

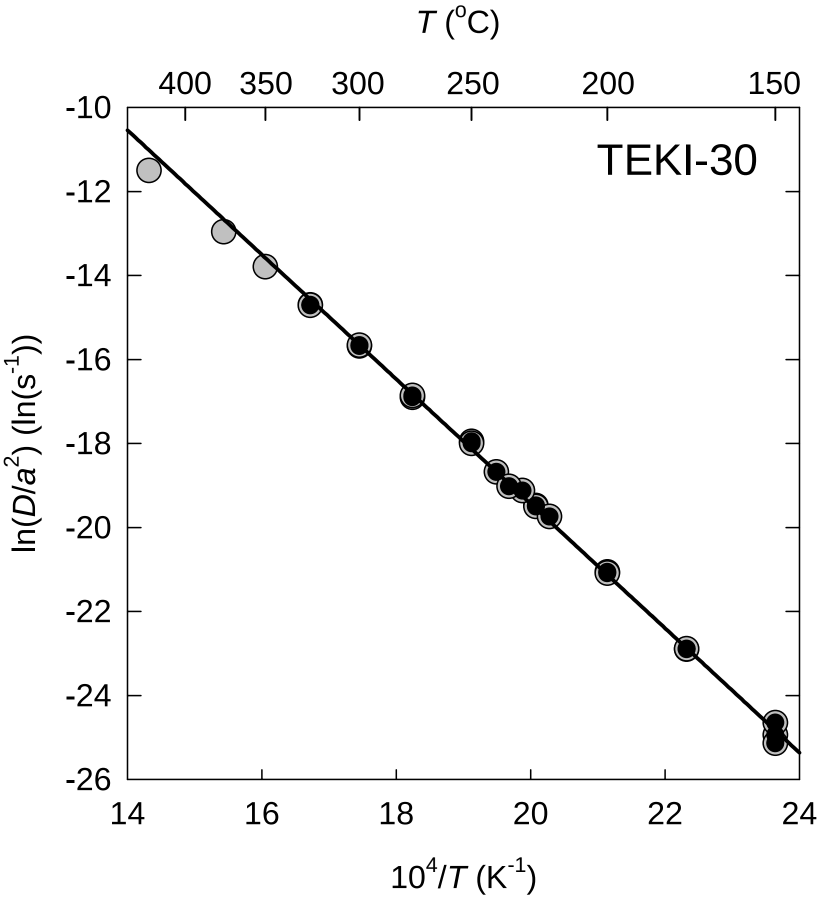

Figure S1-
10 of 26

Helium-3 experiment

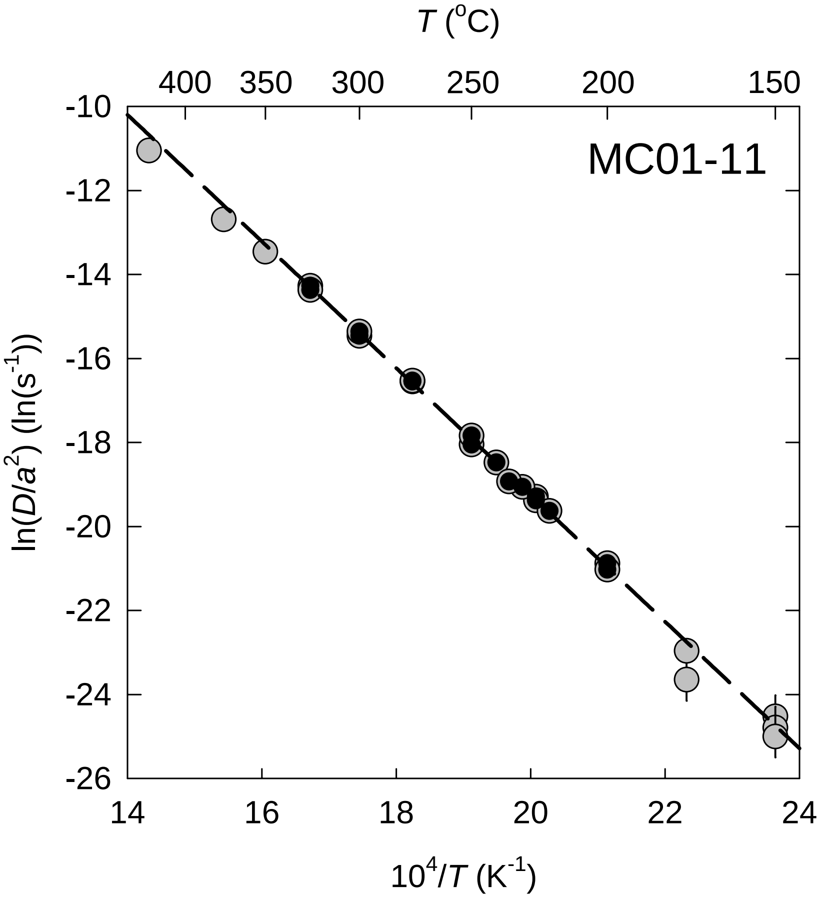

Supplementary figures for "The influence of natural radiation damage on helium diffusion kinetics in apatite"

Figure S1-
11 of 26

Helium-3 experiment

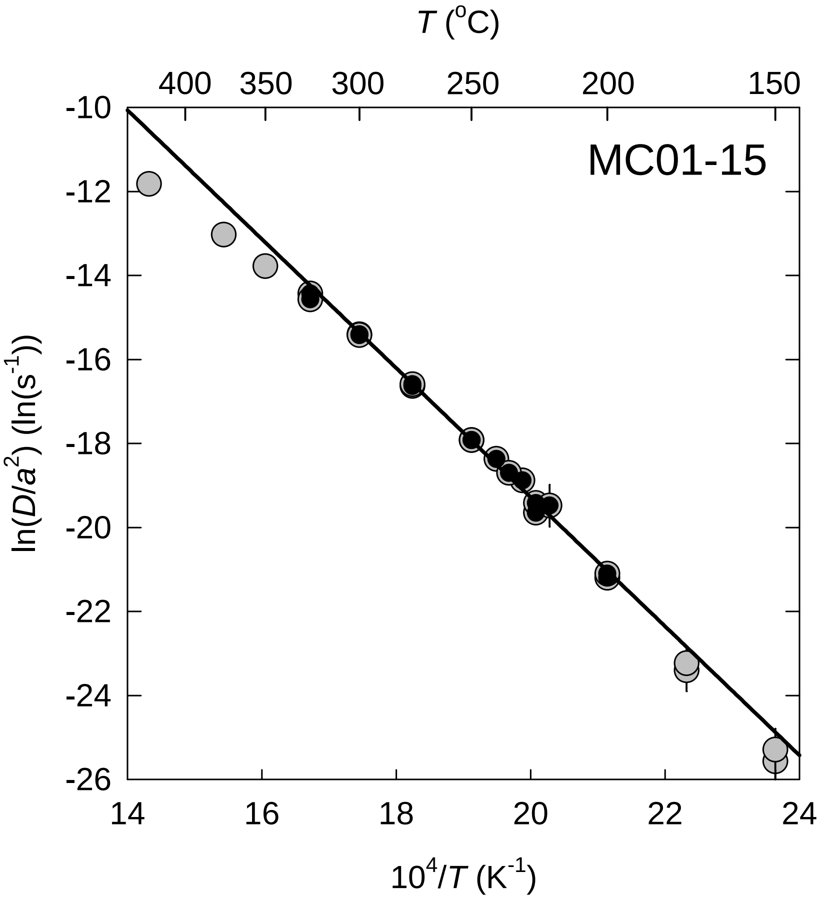

Supplementary figures for "The influence of natural radiation damage on helium diffusion kinetics in apatite"

Figure S1-
12 of 26

Helium-3 experiment

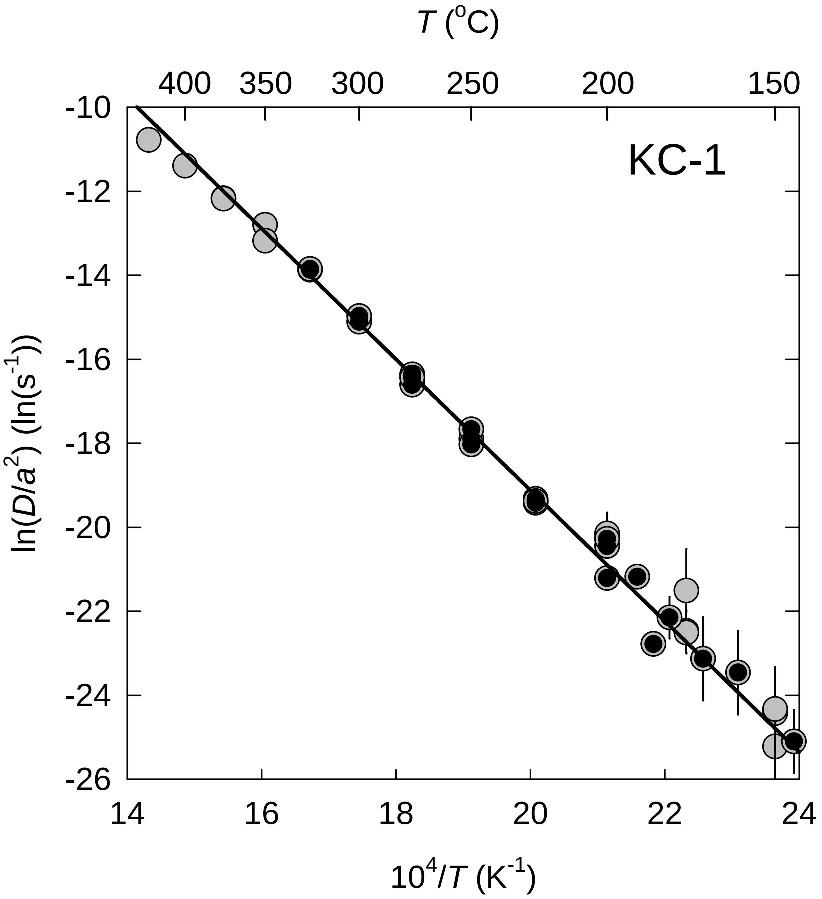

Figure S1-
13 of 26

Helium-3 experiment

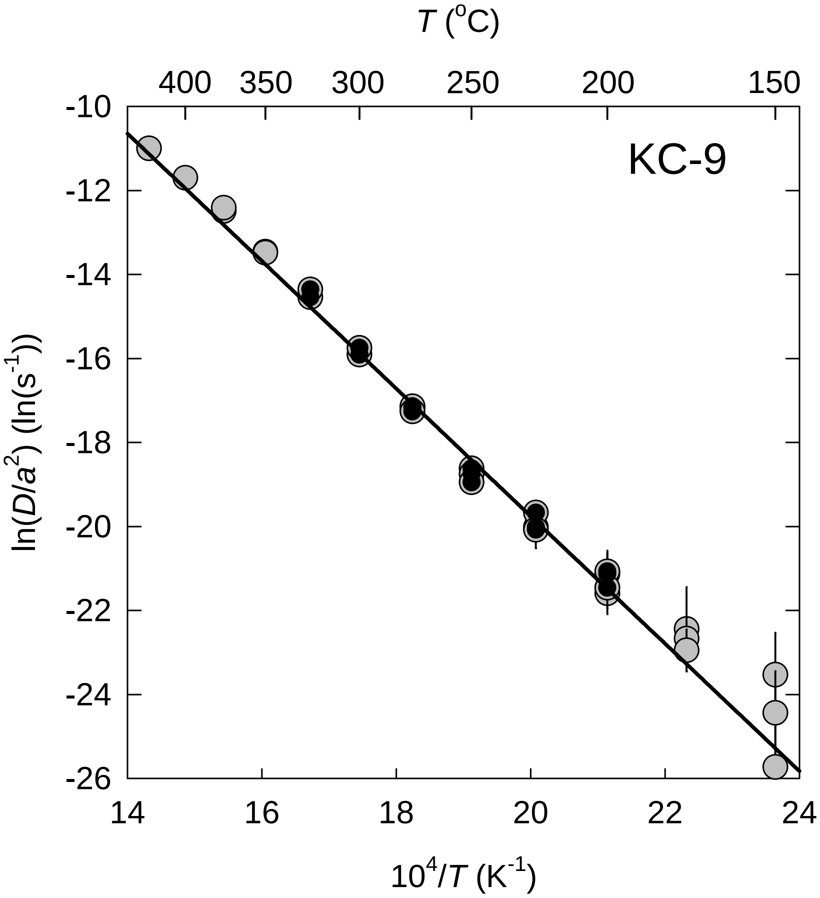

Figure S1-
14 of 26

Helium-3 experiment

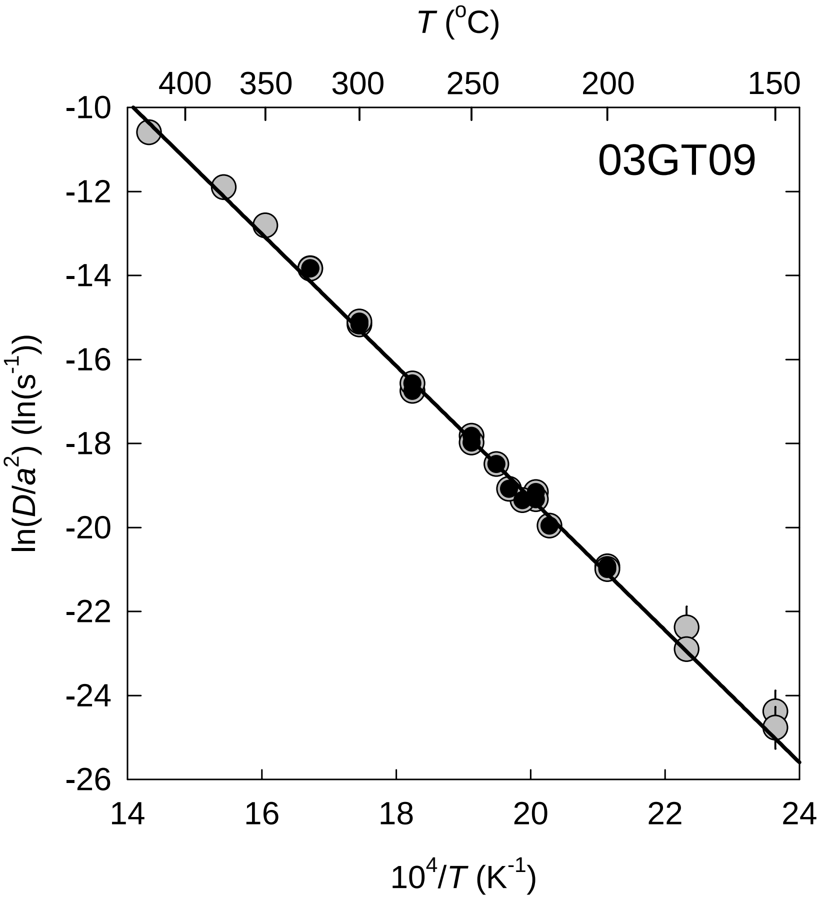

Figure S1-
15 of 26

Helium-3 experiment

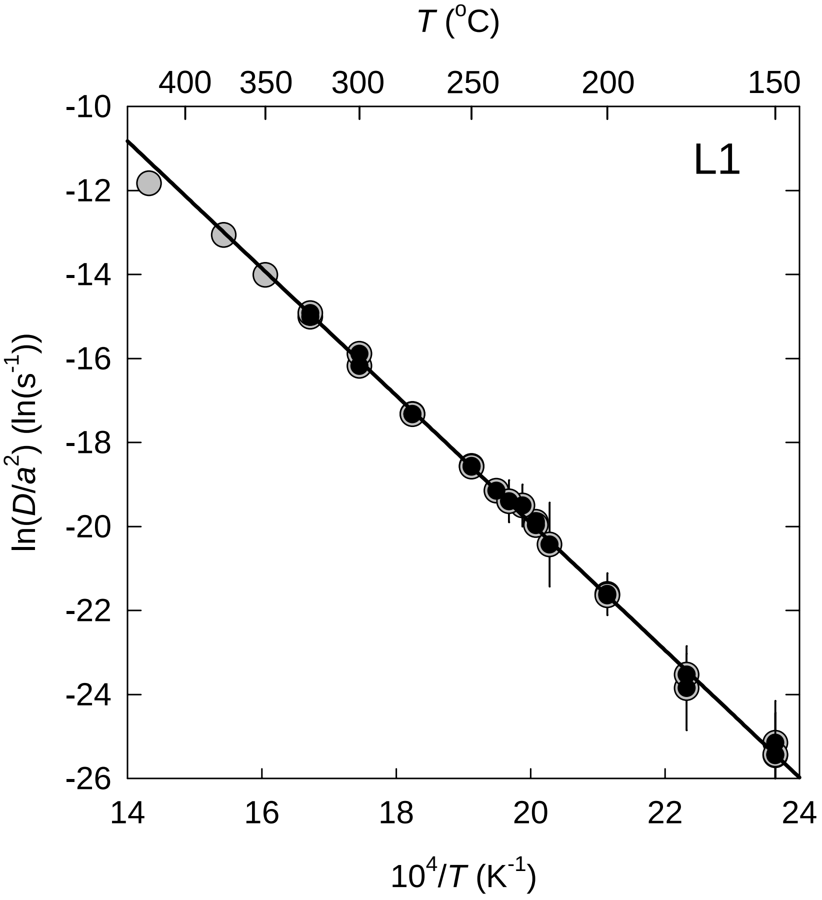

Supplementary figures for "The influence of natural radiation damage on helium diffusion kinetics in apatite"

Figure S1-
16 of 26

Helium-3 experiment

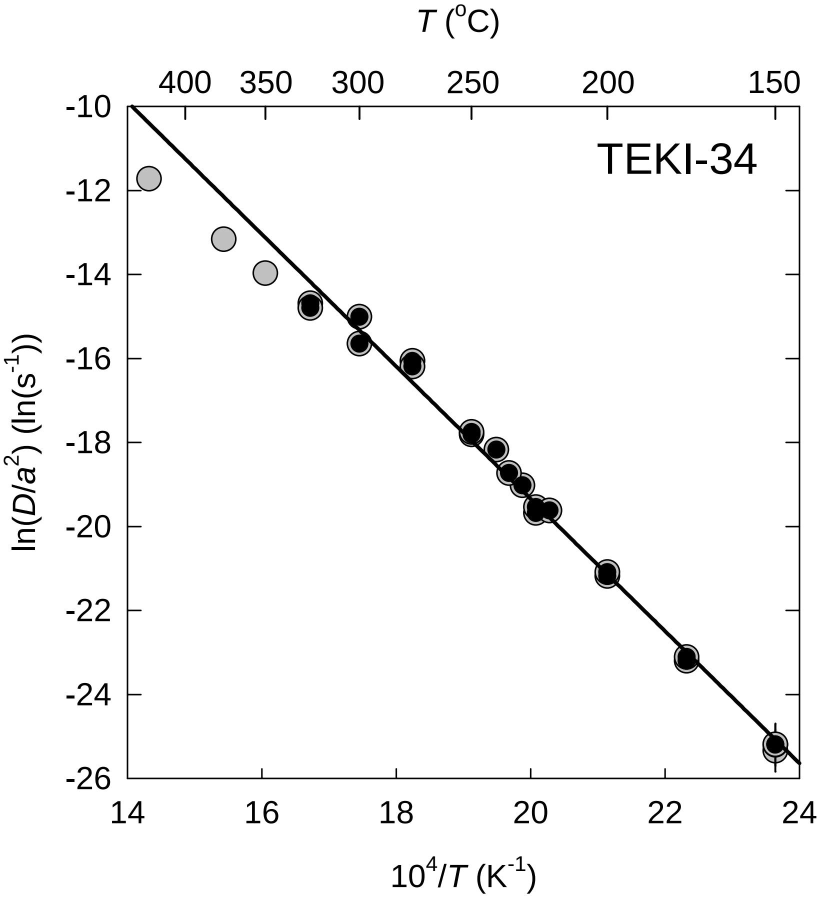

Supplementary figures for "The influence of natural radiation damage on helium diffusion kinetics in apatite"

Figure S1-
17 of 26

Helium-3 experiment

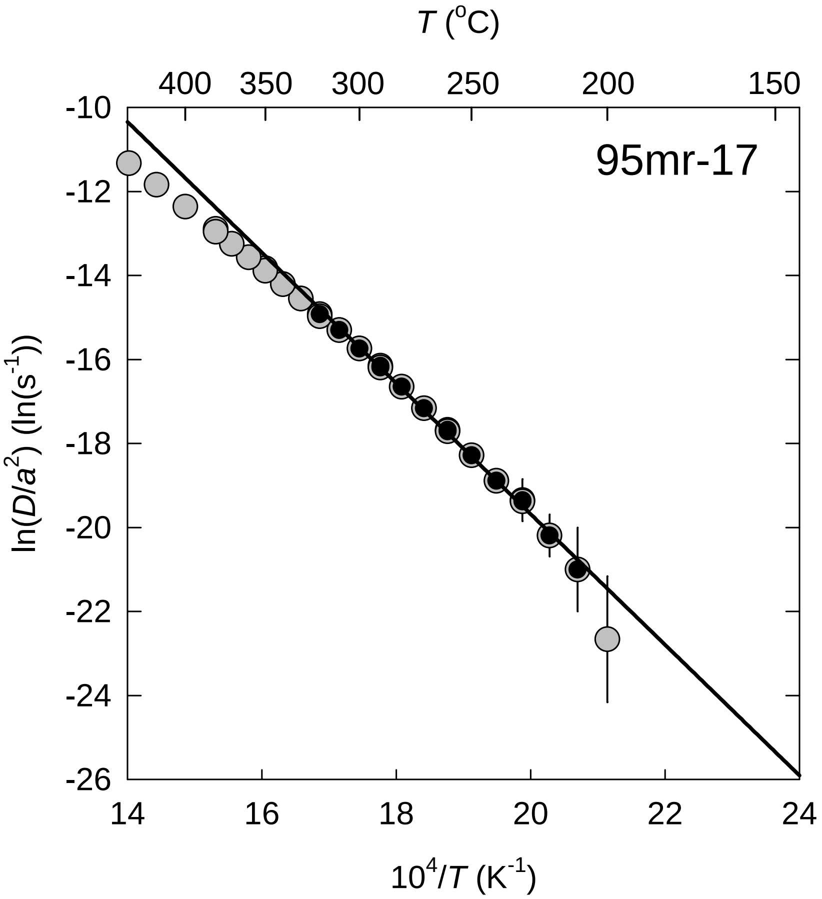

Supplementary figures for "The influence of natural radiation damage on helium diffusion kinetics in apatite"

Figure S1-
18 of 26

Helium-3 experiment

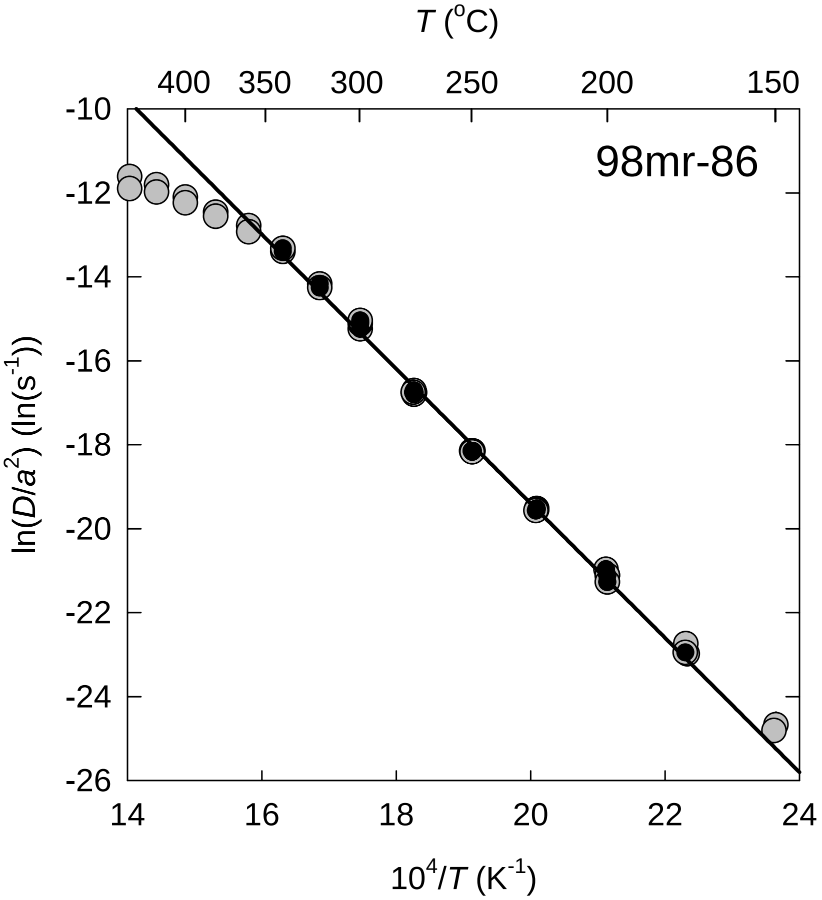

Supplementary figures for "The influence of natural radiation damage on helium diffusion kinetics in apatite"

Figure S1-
19 of 26

Helium-3 experiment

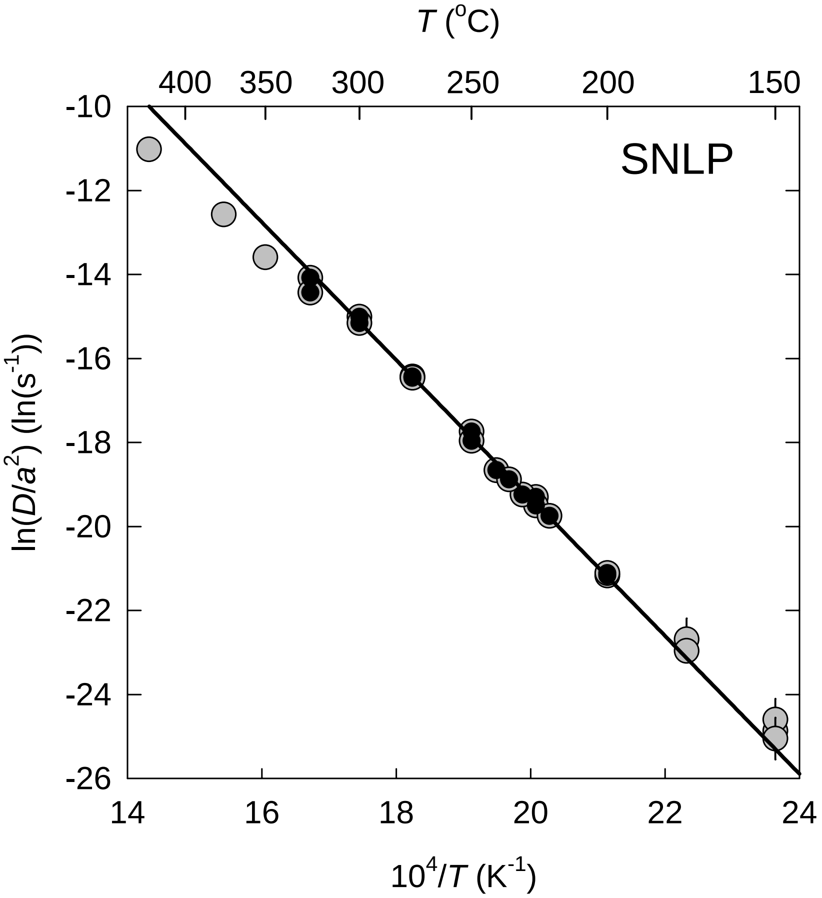

Supplementary figures for "The influence of natural radiation damage on helium diffusion kinetics in apatite"

Figure S1-
20 of 26

Helium-3 experiment

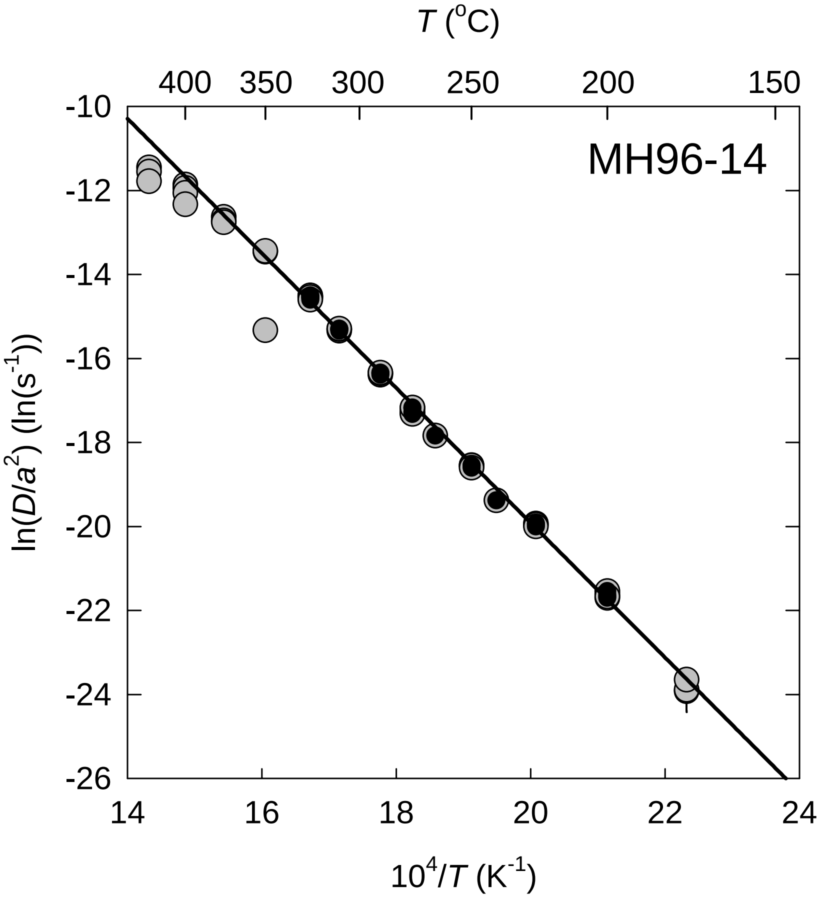

Figure S1-
21 of 26

Helium-3 experiment

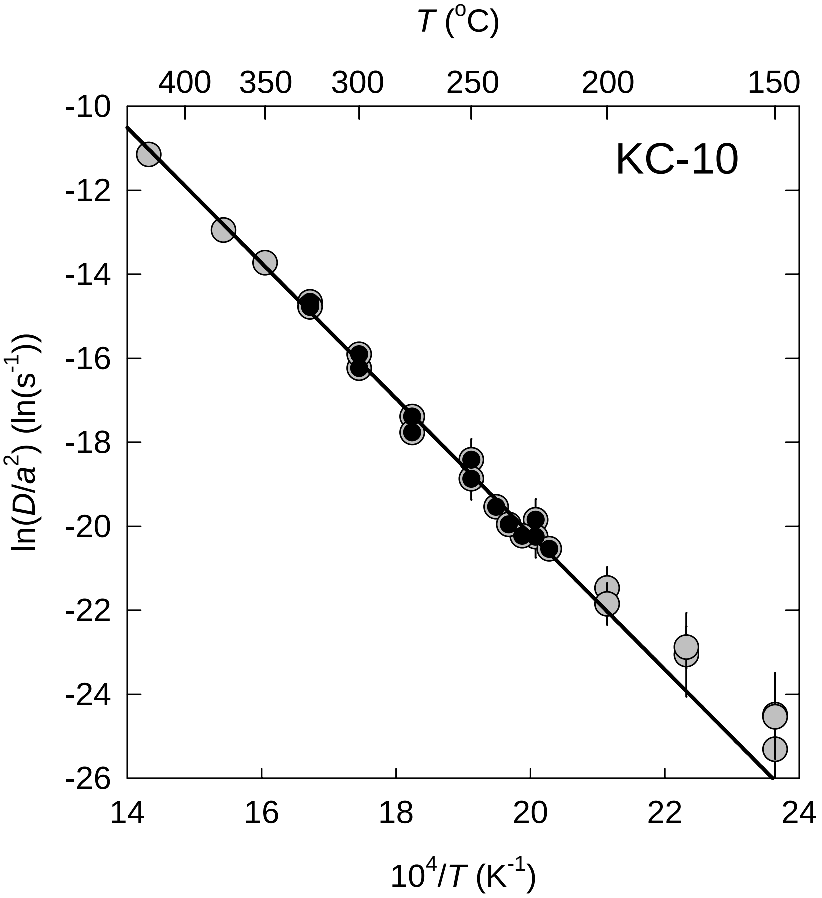

Supplementary figures for "The influence of natural radiation damage on helium diffusion kinetics in apatite"

Figure S1-
22 of 26

Helium-3 experiment

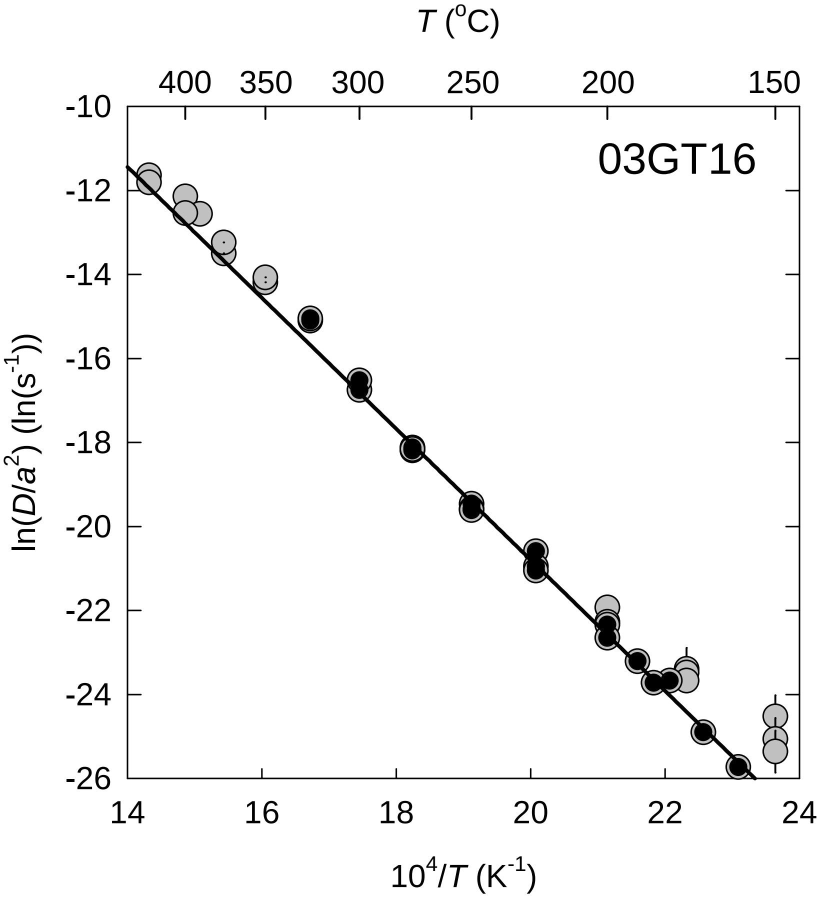

Supplementary figures for "The influence of natural radiation damage on helium diffusion kinetics in apatite"

Figure S1-
23 of 26

Helium-3 experiment

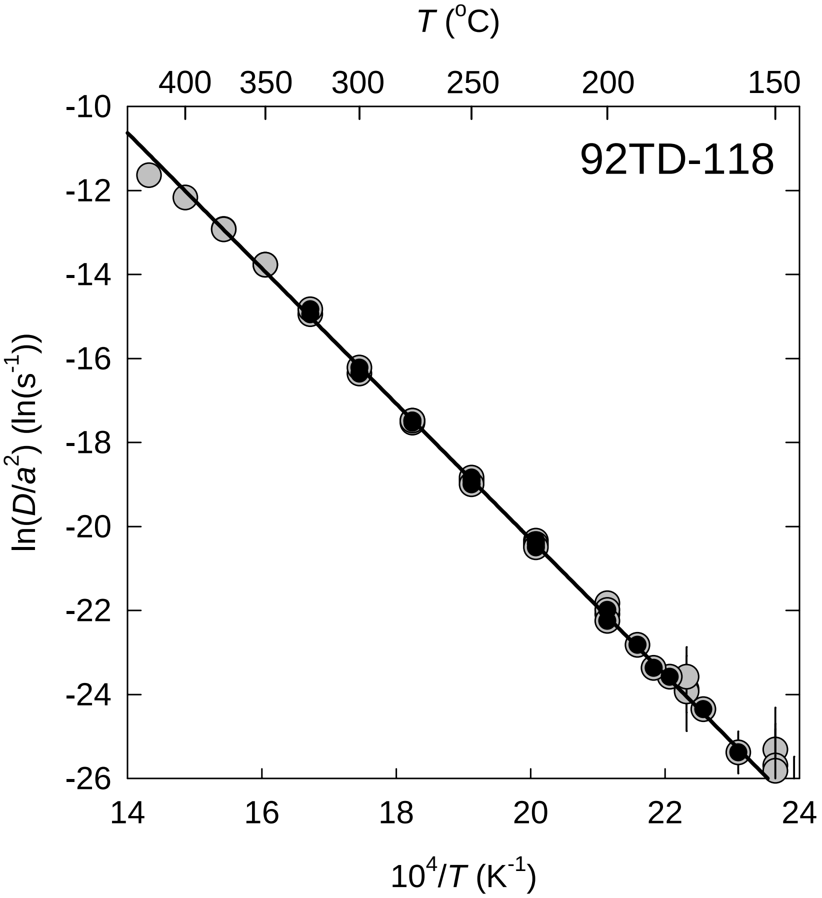

Supplementary figures for "The influence of natural radiation damage on helium diffusion kinetics in apatite"

Figure S1-
24 of 26

Helium-3 experiment

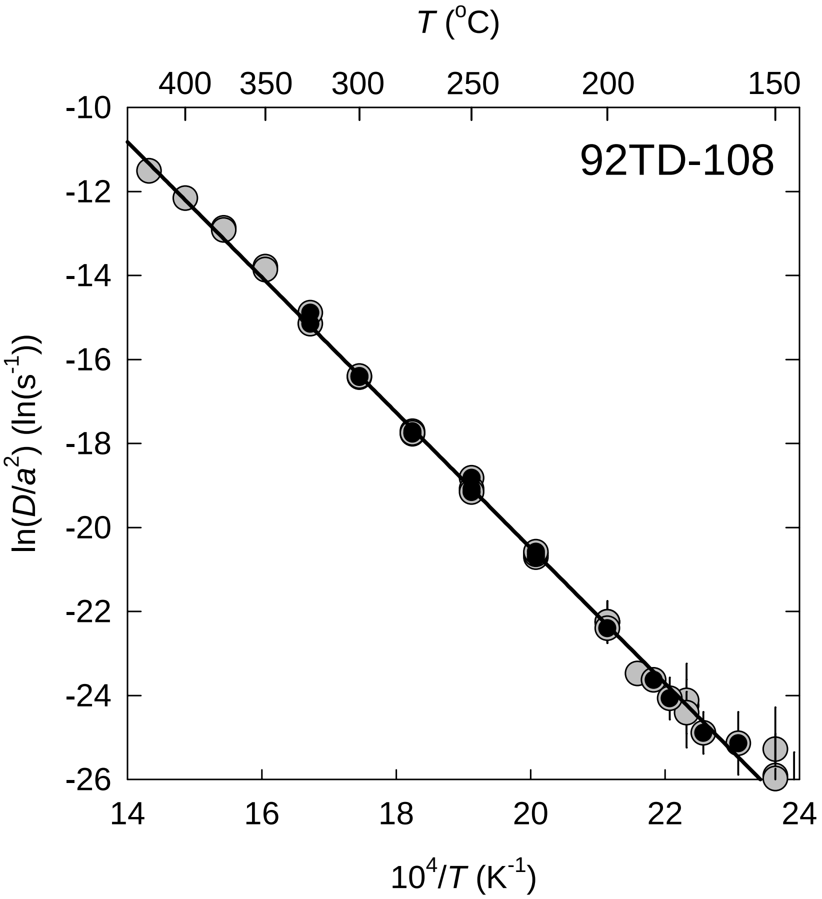

Figure S1-
25 of 26

Helium-3 experiment

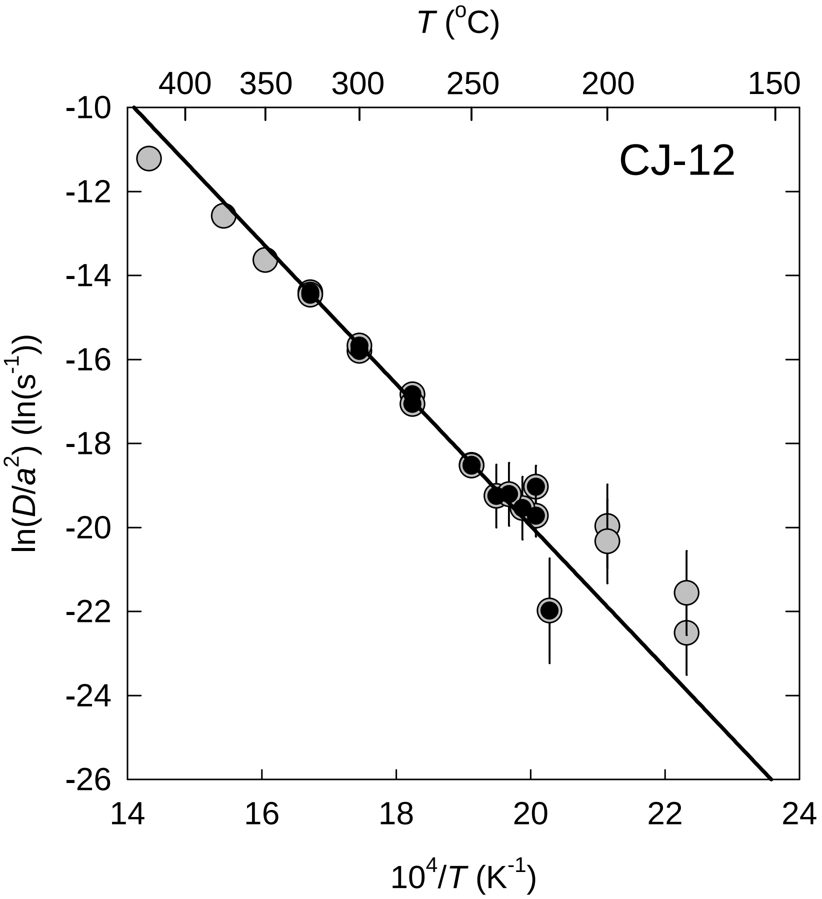

Supplementary figures for "The influence of natural radiation damage on helium diffusion kinetics in apatite"

Figure S1-
26 of 26

Helium-3 experiment

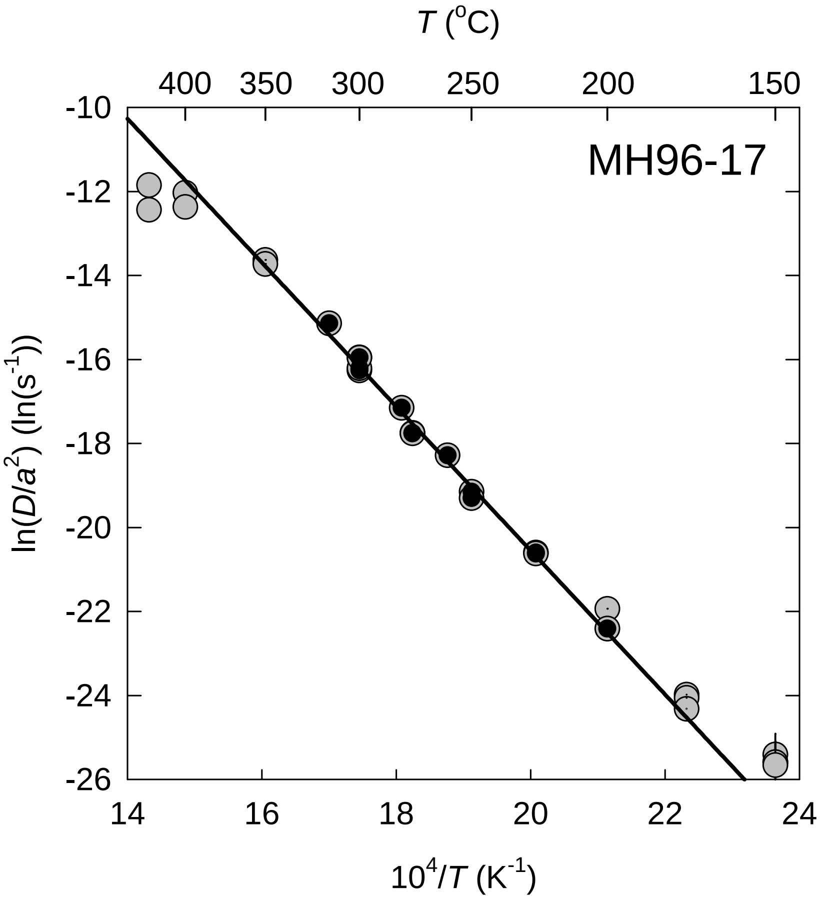

Supplementary figures for "The influence of natural radiation damage on helium diffusion kinetics in apatite"

Figure S2-
1 of 13

Helium-4 experiment

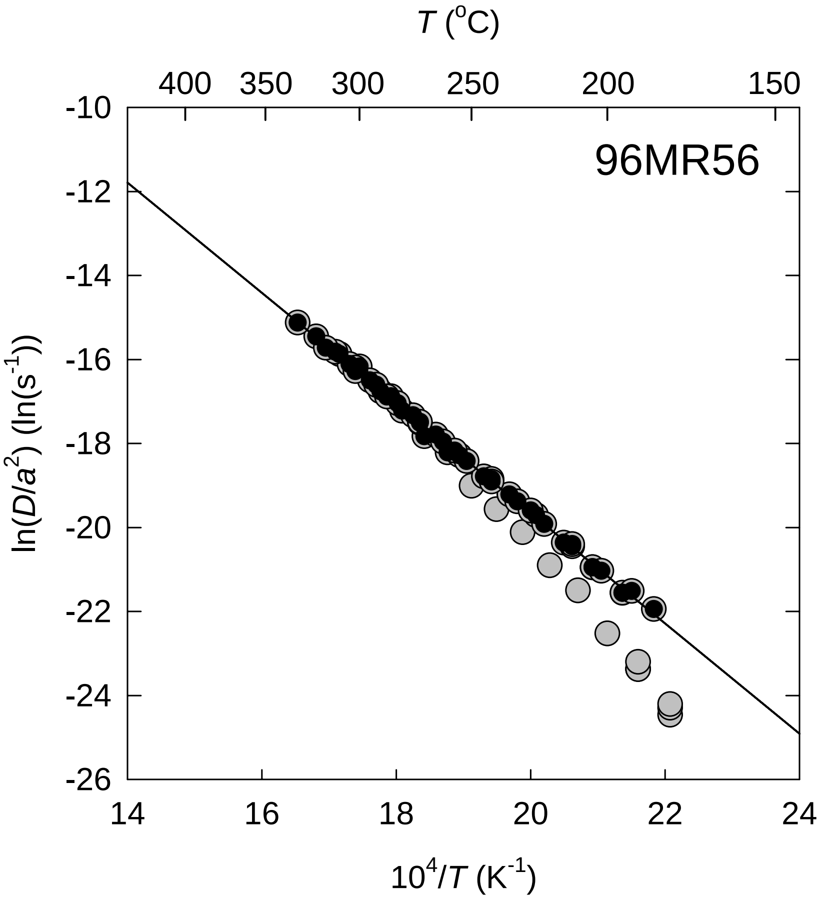

Supplementary figures for "The influence of natural radiation damage on helium diffusion kinetics in apatite"

Figure S2-
2 of 13

Helium-4 experiment

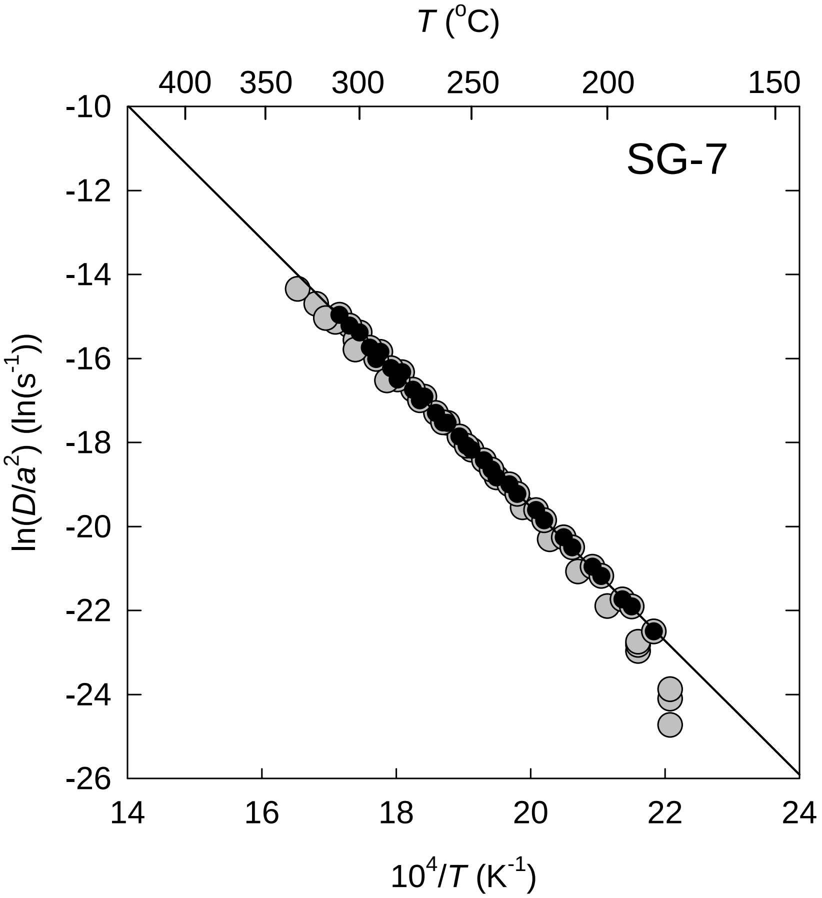

Supplementary figures for "The influence of natural radiation damage on helium diffusion kinetics in apatite"

Figure S2-
3 of 13

Helium-4 experiment

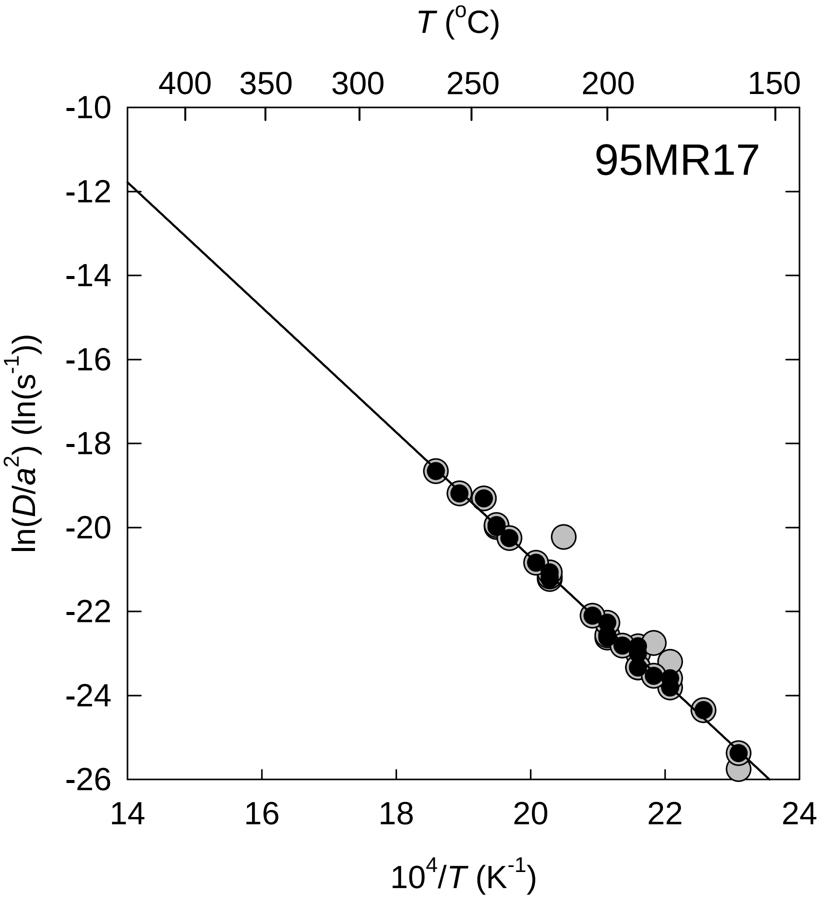

Figure S2-
4 of 13

Helium-4 experiment

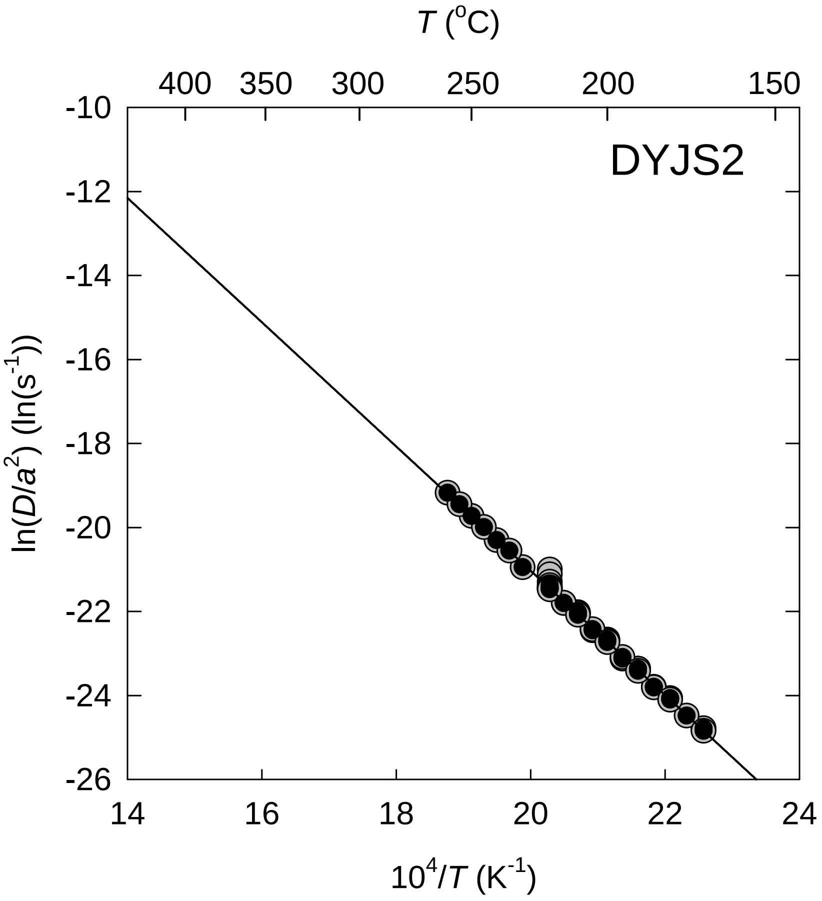

Figure S2-
5 of 13

Helium-4 experiment

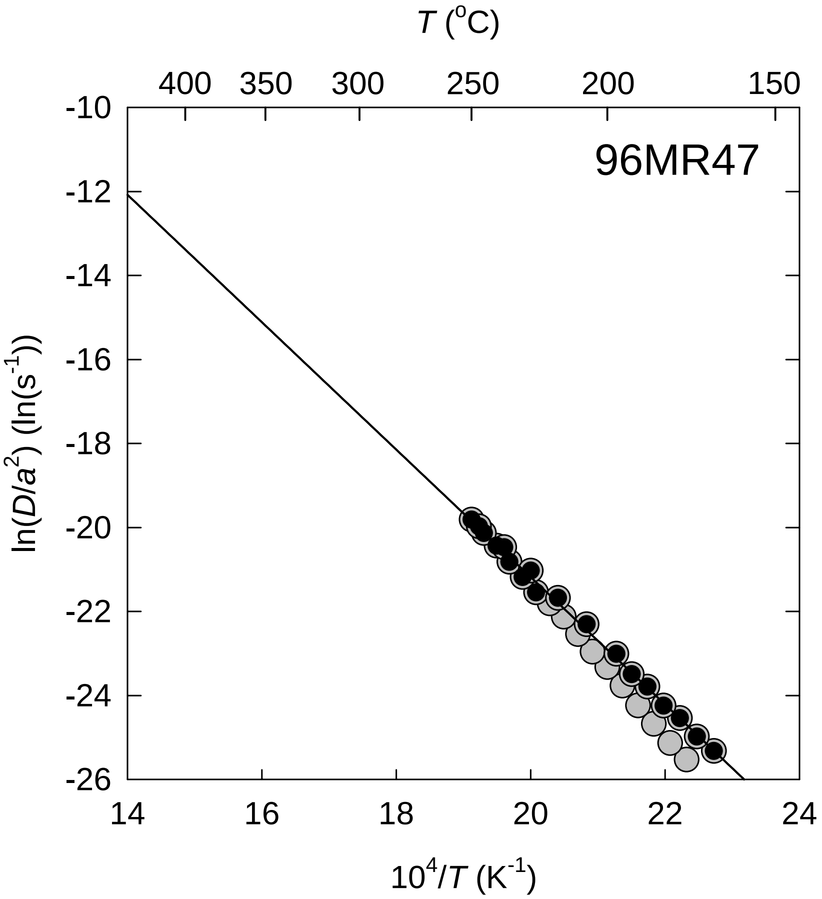

Figure S2-
6 of 13

Helium-4 experiment

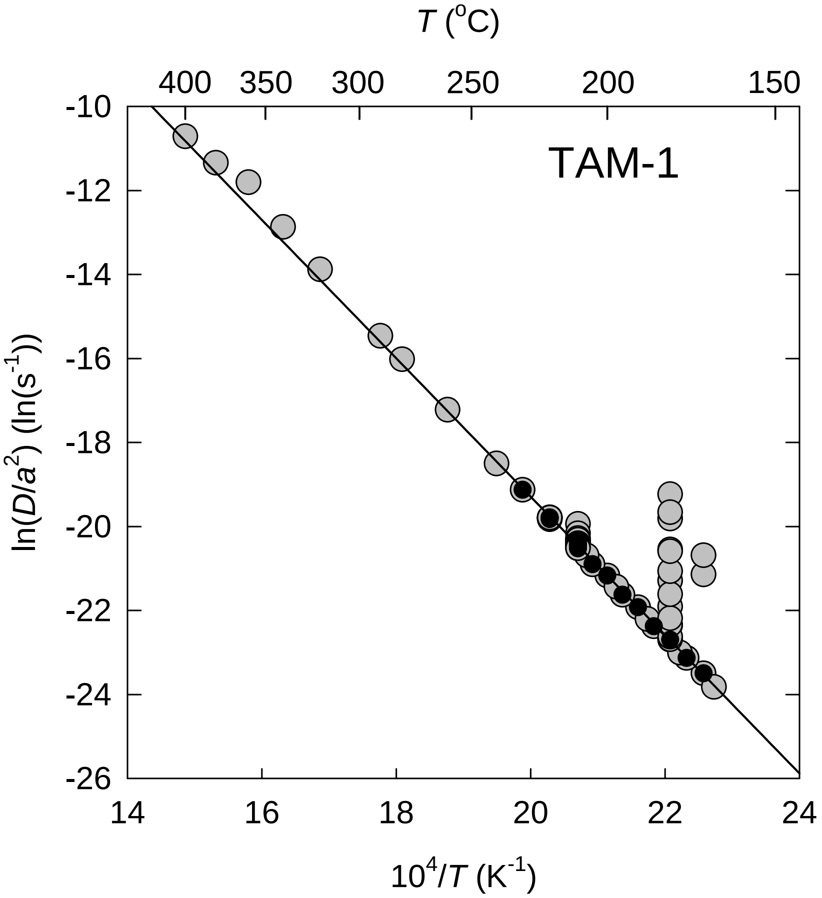

Supplementary figures for "The influence of natural radiation damage on helium diffusion kinetics in apatite"

Figure S2-
7 of 13

Helium-4 experiment

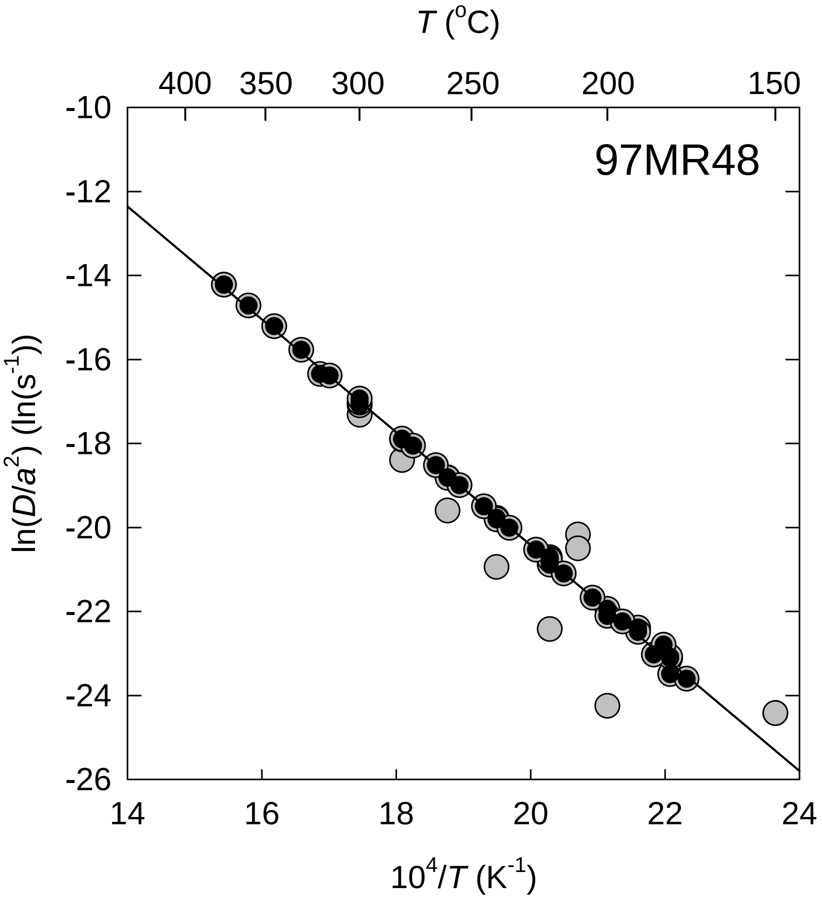

Figure S2-
8 of 13

Helium-4 experiment

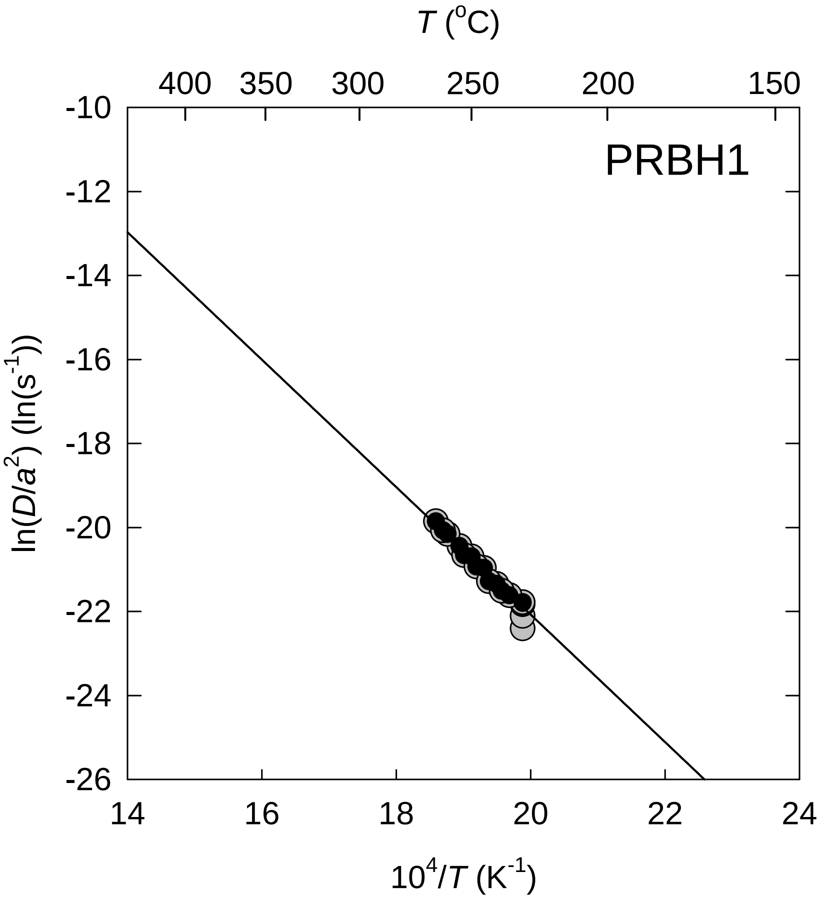

Figure S2-
9 of 13

Helium-4 experiment

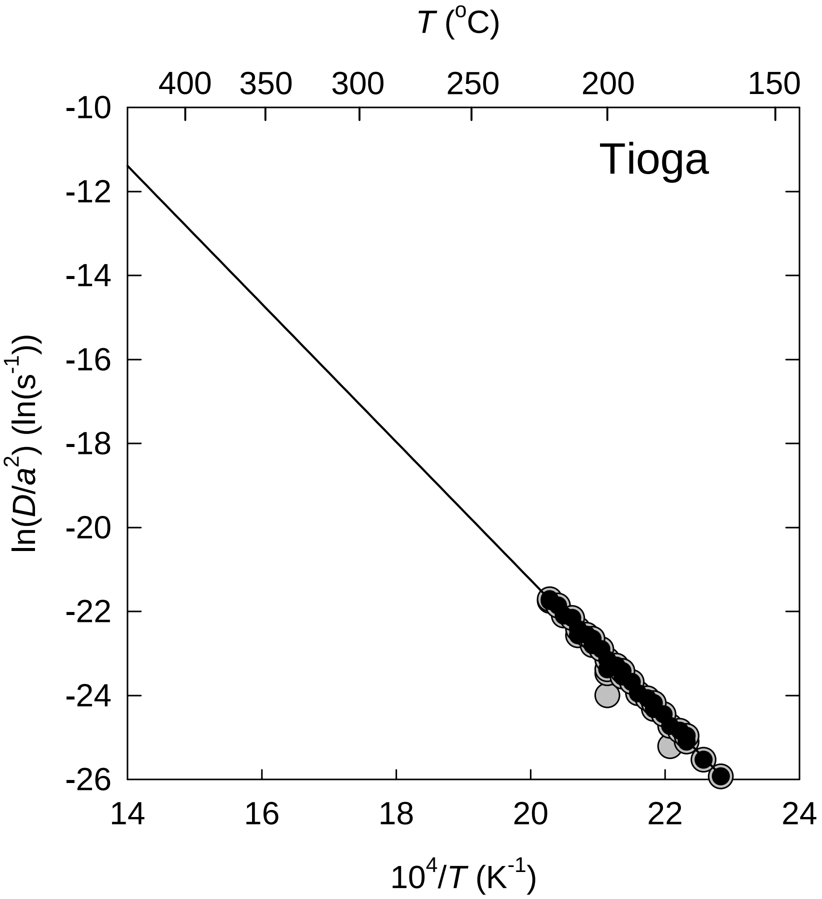

Supplementary figures for "The influence of natural radiation damage on helium diffusion kinetics in apatite"

Figure S2-
10 of 13

Helium-4 experiment

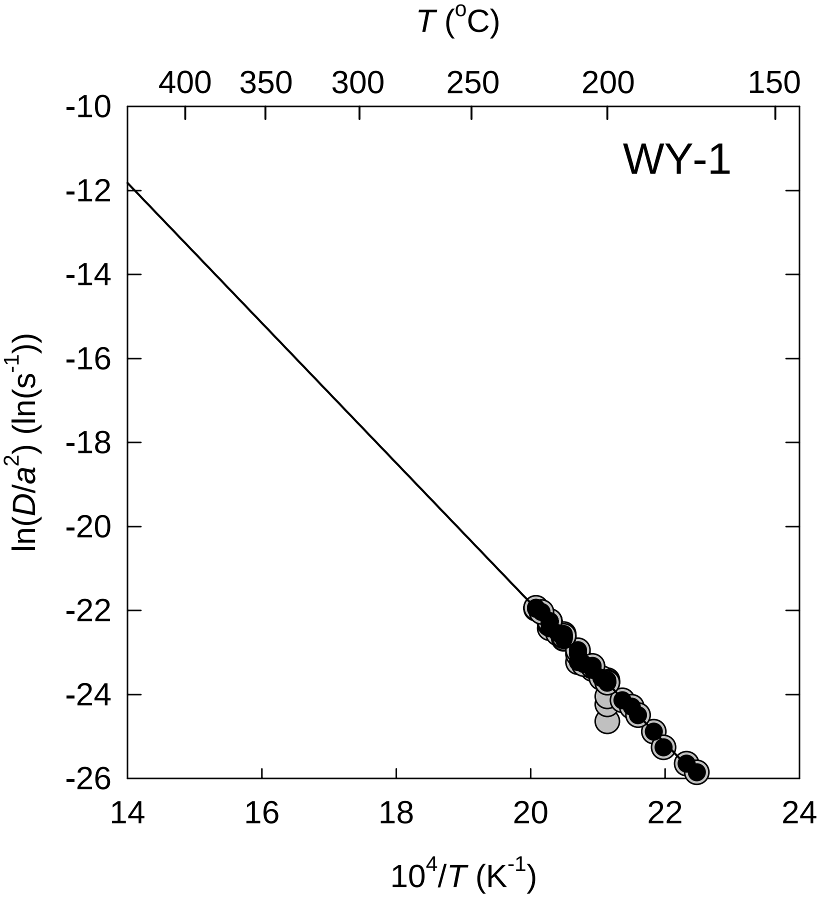

Supplementary figures for "The influence of natural radiation damage on helium diffusion kinetics in apatite"

Figure S2-
11 of 13

Helium-4 experiment

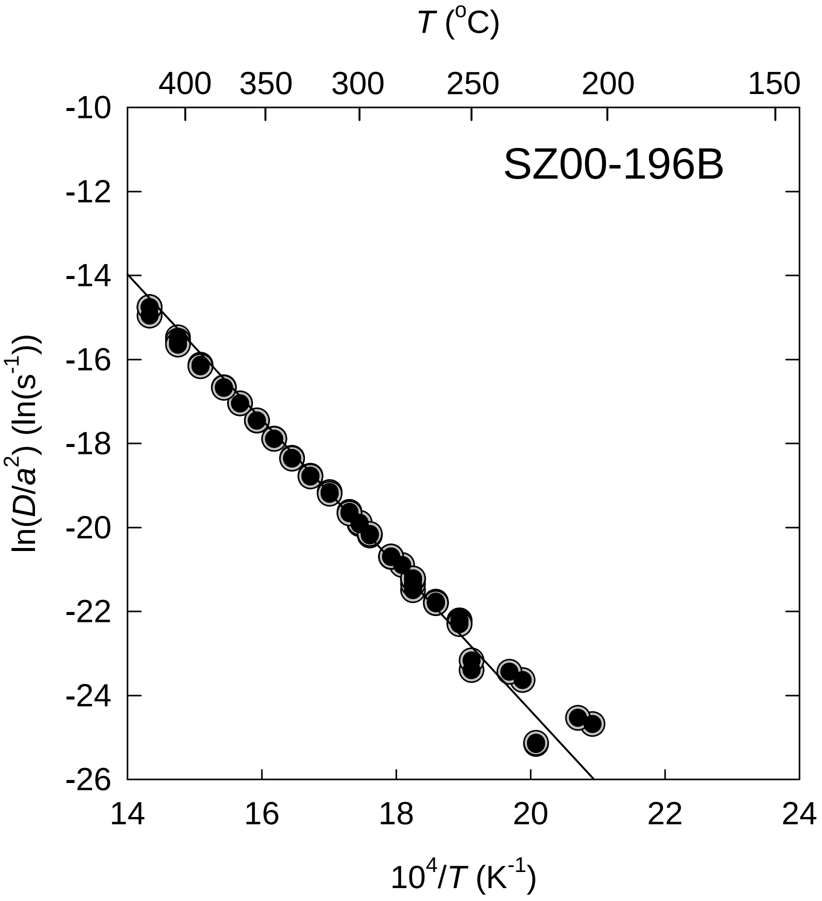

Supplementary figures for "The influence of natural radiation damage on helium diffusion kinetics in apatite"

Figure S2-
12 of 13

Helium-4 experiment

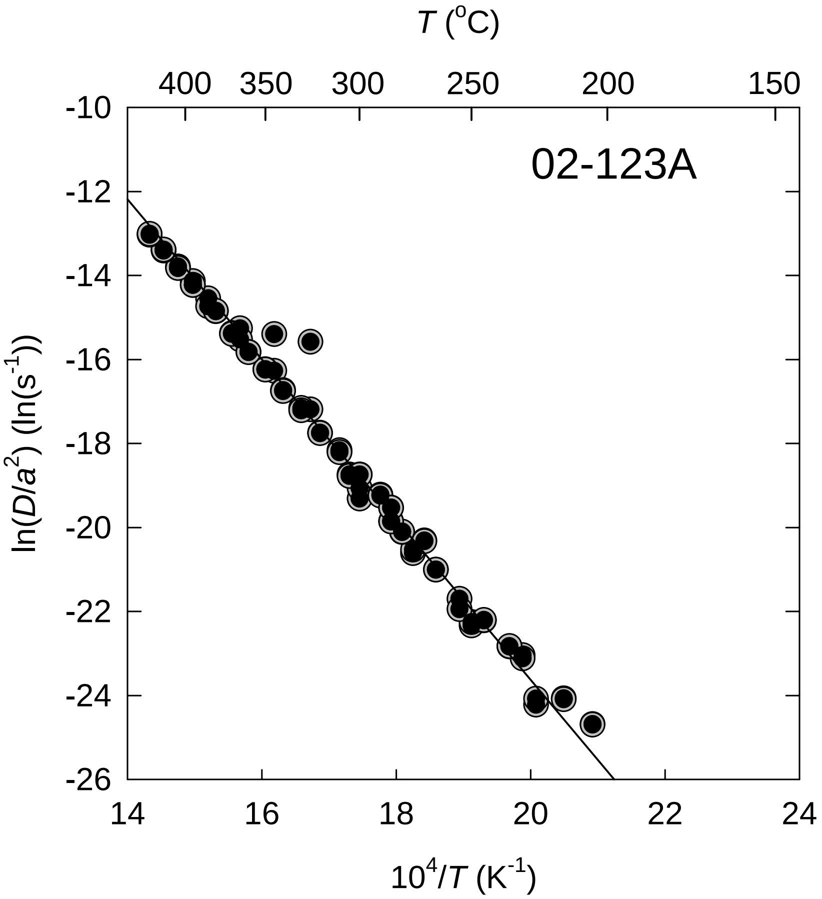

Supplementary figures for "The influence of natural radiation damage on helium diffusion kinetics in apatite"

Figure S2-
13 of 13

Helium-4 experiment

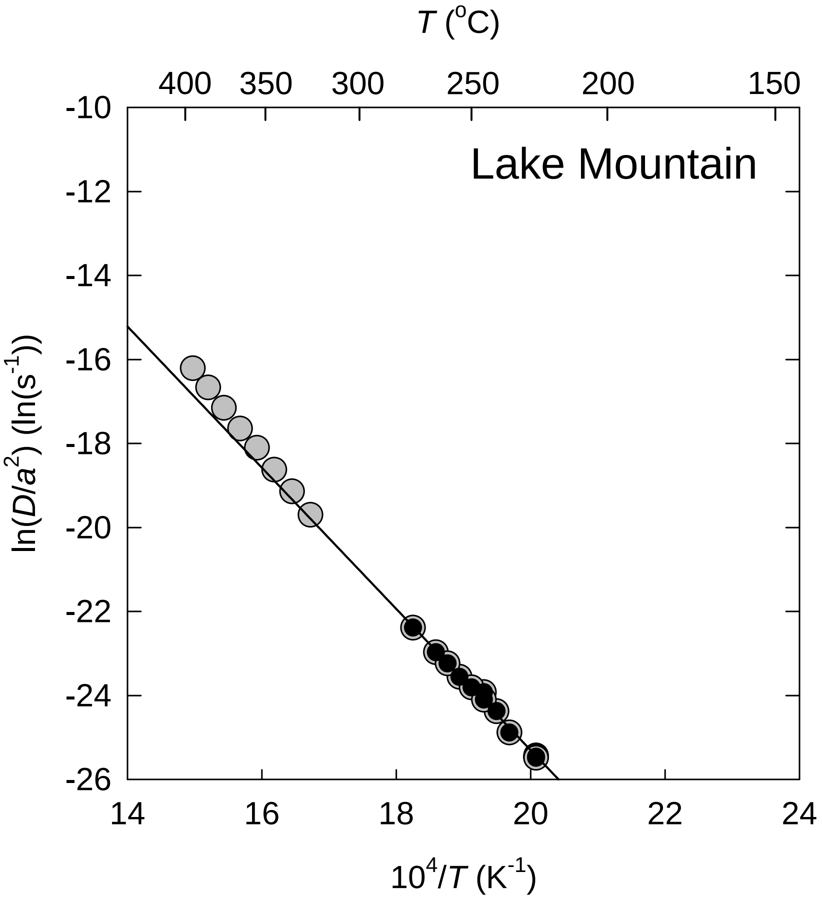

Figure S3 - MLR model predictions

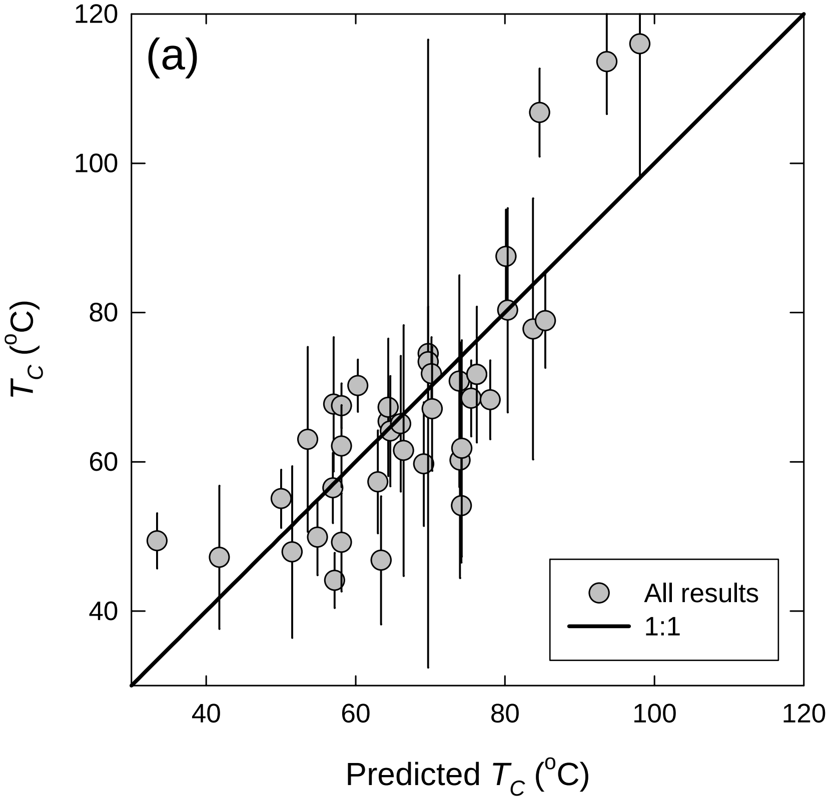

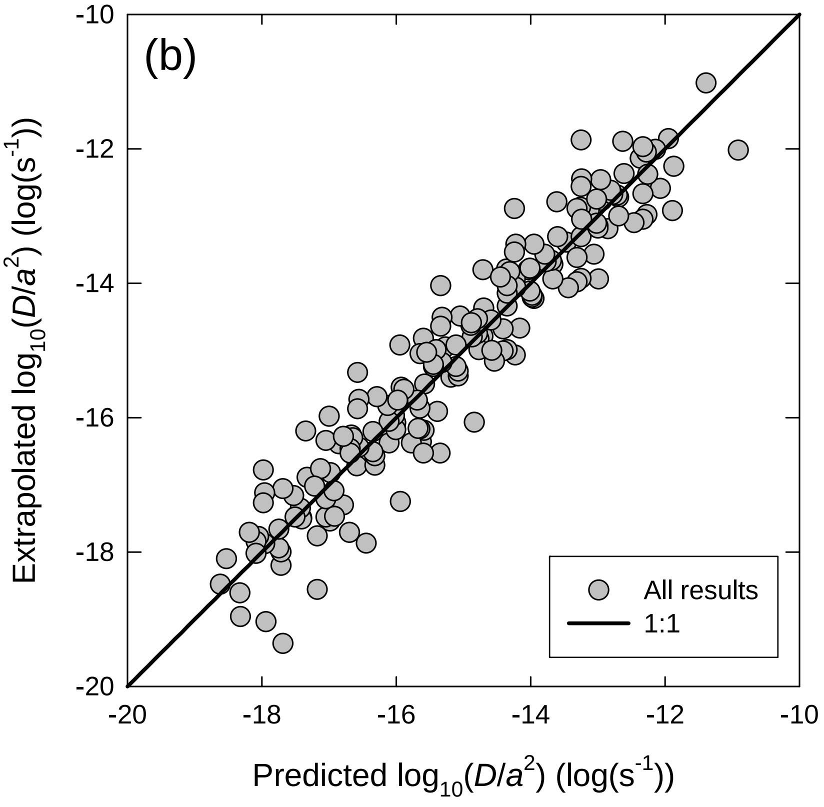

Figure S4- "trapping" model predictions